Journal of Materials Chemistry A

ROYAL SOCIETY OF CHEMISTRY

PAPER

View Article Online
View Journal | View Issue

Check for updates

Cite this: *J. Mater. Chem. A*, 2025, **13**, 38316

Revisiting the original 2003 garnet-like Li-ion conducting solid electrolytes $Li_5La_3M_2O_{12}$ (M = Nb, Ta, Nb/Ta): a look into phase formation and the identification of carbonate and alumina contamination

Heather A. Ritchie, Ioanna M. Pateli, Oxana V. Magdysyuk, Aaron B. Naden, Heitor S. Seleghini, Federico Grillo, Gavin Peters, Sharon E. Ashbrook, John T. S. Irvine and Venkataraman Thangadurai *

Garnet-type electrolytes are a promising class of solid-state oxide materials for next-generation lithium batteries. In this study, parent-phase garnets, $Li_5La_3M_2O_{12}$ (M = Nb, Ta, Nb/Ta), were synthesised *via* solid-state reaction at 900 °C and 1100 °C, enabling comprehensive structural and chemical stability characterisation. Powder X-ray diffraction (PXRD) and Raman spectroscopy confirmed single-phase garnets with $Ia\bar{3}d$ symmetry, while scanning electron microscopy (SEM) imaging revealed improved densification at 1100 °C. Electrochemical impedance spectroscopy showed the high ionic conductivities of 4.8×10^{-5} S cm^{-1} at 55 °C for Nb and Ta co-substituted $Li_5La_3NbTaO_{12}$ prepared at 1100 °C. X-ray photoelectron spectroscopy and thermogravimetric analysis identified a surface lithium carbonate layer formed under ambient conditions, which was not discussed in the original garnet reported in 2003. Solid-state nuclear magnetic resonance spectroscopy provided an insight into the lithium environment in the surface and bulk of the samples and confirmed aluminium contamination in samples sintered at the base of alumina crucibles at 1100 °C, with $LaAlO_3$ identified as the dominant secondary phase, corroborated by PXRD, SEM, and energy dispersive X-ray spectroscopy analysis. Nb-based garnet showed the most severe reaction with the alumina crucible. The use of a sacrificial mother powder of targeted garnet oxides, an approach commonly used for the preparation of Li-garnets, or sintering at 900 °C effectively reduced Al contamination. This work delivers a detailed evaluation of the parent-phase garnet, offering renewed insights into phase and structure two decades on from its initial development in 2003.

Received 25th August 2025
Accepted 1st October 2025

DOI: 10.1039/d5ta06905j

rsc.li/materials-a

1. Introduction

The capabilities of lithium-ion batteries (LIBs) have advanced significantly since their first commercial use in the 1991 Sony camcorder. While conventional LIBs have continued to push the boundaries of energy storage, they still face several limitations that must be overcome to meet rising energy demands and support the global shift toward sustainable energy technologies. One promising route for LIB innovation lies in the development of new electrolyte materials, by replacing the traditional liquid electrolyte with an ionically conductive solid, which could enable next-generation battery technologies capable of higher energy and power densities.[1] Solid-state electrolytes (SSEs) offer numerous advantages over conventional organic liquid electrolytes, including improved safety. Inorganic oxide-based SSEs exhibit high thermal stability and significantly reduce the risk of thermal runaway, which is a critical safety concern in current LIB systems.[2] Additionally, SSEs reduce unwanted chemical reactions between electrodes, which can occur in liquid systems, where soluble species are able to migrate across the cell, leading to material loss, self-discharge, and long-term degradation.[3] Over the years, extensive research has led to the exploration of many inorganic SSEs such as oxides, halides, and sulfides, each with distinct advantages.[2] Among them oxide-based electrolytes have emerged as one of the most favourable classes for future solid-state lithium battery development, including the NASICON, perovskite and garnet-type electrolytes.[2] Garnet-type materials with excess lithium compared to the ideal stoichiometry have gained significant attention in the solid-state battery field due to their high ionic conductivities. The most extensively studied Li-conducting garnets typically contain between five and seven lithium atoms per formula unit and are commonly known as Li-stuffed or Li-rich garnets.[4]

EaStCHEM, School of Chemistry, University of St Andrews, North Haugh, St Andrews, KY16 9ST, UK. E-mail: vt36@st-andrews.ac.uk

In 2003, Thangadurai *et al.*[5] reported lithium-ion conducting original garnet-type oxides with nominal composition $Li_5La_3M_2O_{12}$ (M = Nb, Ta). This work highlighted that $Li_5La_3Ta_2O_{12}$ is chemically stable to lithium metal, which is a major advantage over many of the other promising solid electrolytes, such as $La_{0.67-x}Li_{3x}\square_{0.33-2x}TiO_3$ ($\square$ = A-site vacancy; $x = 0.1$ member exhibits bulk ionic conductivity of about 10^{-3} S cm^{-1} at room temperature) and $Li_{1.3}Ti_{1.7}Al_{0.3}(PO_4)_3$.[5] Cussen demonstrated through neutron diffraction study the three-dimensional network of Li diffusion within the garnet structure and highlighted the role of partially occupied octahedral sites in facilitating Li mobility.[6] The combination of high ionic conductivity, chemical stability, and compatibility with lithium metal attracted significant interest, and over two decades on from their initial conception, the Li_5-composition has earned the title of 'parent-phase lithium garnet' electrolytes. Cerium-doping in the parent phase $Li_5La_3Nb_2O_{12}$ was shown to enhance ionic conductivity by nearly two orders of magnitude, representing the highest value reported among the Li_5 garnet family.[7] The development of further garnet-like structures with enhanced conductivities was achieved by partially substituting the trivalent La^{3+} ions with divalent cations, leading to an increased lithium-ion concentration within the structure. This modification gave rise to a new subset of garnet-type electrolytes with the general formula $Li_6ALa_2M_2O_{12}$ (A = Mg, Ca, Sr, Ba, $Sr_{0.5}Ba_{0.5}$).[8] A breakthrough in highly conducting garnet-type realised in 2007 when Murugan, Thangadurai and Weppner reported the cubic $Li_7La_3Zr_2O_{12}$ (LLZO), which showed a bulk conductivity of 3×10^{-4} S cm^{-1} at 25 °C, over an order of magnitude higher ionic conductivity than that of parent $Li_5La_3M_2O_{12}$ garnets.[9] Karasulu *et al.*[10] used experimental and computational *ab initio* analysis to understand the structure of doped and undoped cubic LLZO and demonstrated that Al and Ga dopants preferentially occupy Li1 sites in garnet, giving rise to distinct NMR signatures associated with local distortions.

Following this discovery, subsequent studies reported the formation of a less conductive tetragonal phase when sintering was performed at lower temperatures and in Pt crucible,[11] indicating that the garnet-type structure is highly dependent on both the synthesis and processing conditions. The development of the Li_7-phase marked a significant advancement, offering enhanced ionic conductivity and sparking a wave of research into the optimisation and application of garnet-type electrolytes, a field that is actively explored today.[12–14] The surface chemistry of an SSE directly impacts the solid–solid interfacial properties in a solid-state battery, which in turn can significantly impact the battery performance. Initially, garnet-type electrolytes were thought to be chemically stable in ambient conditions; however, it has now been highlighted that surface layers of Li_2CO_3 formation in air results in low ionic conductivities and low densities.[15] Further, the Li_2CO_3 layer is known to affect the wettability of Li metal on the electrolyte surface,[16] which creates challenges during cell assembly.

The aim of this revisitation is to conduct a comprehensive investigation of the parent-phase garnet electrolyte $Li_5La_3M_2O_{12}$ to build a deep fundamental understanding of its structural, chemical, and electrochemical properties. This study offers a renewed evaluation of this emerging material through the synthesis of original $Li_5La_3M_2O_{12}$ and 1 : 1 solid solution of $Li_5La_3Nb_2O_{12}$ and $Li_5La_3Ta_2O_{12}$ and revisits the material purity through state-of-the-art solid-state characterisation methods. Whilst investigating surface contamination that arises during processing, particularly Li_2CO_3 formation due to air exposure, and examining intrinsic Al-doping introduced from alumina crucibles during high temperature processing, which have not been as widely studied for the parent phase Li_5-composition garnet, unlike Li-stuffed LLZO and its derivatives.

2. Experimental section

2.1 Synthesis

Standard solid-state synthesis procedure was followed to prepare the garnet materials. High purity (>99%) Li_2CO_3, La_2O_3 (pre-dried at 900 °C for 10 hours), Nb_2O_5 and Ta_2O_5 were obtained from Thermo Scientific (UK) as precursor materials. The required stoichiometric amounts of each material, including a 10 wt% excess of Li_2CO_3 (to account for lithium volatilisation upon heating), were mixed in propan-2-ol and roller milled with 5 mm diameter zirconia balls overnight. After evaporation of the solvent at room temperature, the powder was heated to 750 °C in air for 10 hours, then cooled down to room temperature. The calcined powder was roller milled again in propan-2-ol with 5 mm zirconia beads, and the resultant powders were further heated in air (900–1100 °C) with a heating and cooling rate of 5 °C per minute for 24 h. An intermediate milling step was conducted between any successive heating steps and powders were pressed into 13 mm pellets by uniaxial press before the final sintering step.

2.2 Characterisation by diffraction

Ex situ powder X-ray diffraction (PXRD) measurements at room temperature were performed on PANalytical Empyrean diffractometers, equipped with a solid-state X'Celeration detector, using monochromatic Cu-radiation. Measurements were made in the reflection geometry using flat sample holders. The samples were in either powder or pellet form. *In situ* high-temperature PXRD measurements were performed at variable temperatures using monochromatic Mo-radiation at STOE diffractometer, in the transmission geometry with a linear single-photon counting detector Mythen (DECTRIS). A high-temperature reaction furnace HT2 (STOE) was used with sapphire capillary tubes, containing up to 1 cm length of sample in the middle of the tube (ID approx. 1 mm), which was restricted on both sides by high-temperature quartz wool to prevent the movement of the sample. The measurements were performed under a very low Ar flow to create an almost static inert atmosphere. Program Topas Academic V7 [17] was used for Rietveld refinement analysis.[18,19]

2.3 Characterisation by spectroscopy methods

Room-temperature Raman spectra were collected with a 532 nm wavelength laser in the Renishaw inVia™ confocal Raman microscope, with 1800 lines per mm holographic grating.

Optical microscope with Leica 50× objective lens was used to focus on the samples, and the spectra were collected at 20 random spots on the surface of the sample with various μm distance between them and the average of these points was used in the graphs. Laser exposure time on the samples was 10 seconds, 5% of the laser power was used and 2 accumulations for each point were conducted to increase signal to noise ratio.

Scanning electron microscopy (SEM) images were obtained using the JSM-IT800 Schottky Field Emission Scanning Electron Microscope by JEOL coupled with JEOL Energy Dispersive X-ray Spectrometer (EDS). Images captured in both secondary and back-scattered electron detectors were made using 5 kV and 10 mm working distance. For elemental composition analysis, 15 kV and analysis current mode were used.

X-ray photoelectron spectrometry (XPS) measurements were collected in an ultrahigh vacuum, with base pressure *ca.* 1×10^{-10} mbar, chamber using a Kratos Axis Ultra DLD photoelectron spectrometer with monochromatic Al Kα (1486.6 eV) anode operating at 4 mA × 15 kV. The system was operated in hybrid mode with the slot aperture, giving a measuring area of *ca.* 700 micron × 300 micron. Charge compensation was used during data collection; the binding energy (BE) scale was referenced to adventitious carbon species at 285.0 eV and BE values are reported ± 0.1 eV. Peak fitting was carried out using the CasaXPS software,[20] with Kratos supplied sensitivity factors, using Gaussian–Lorentzian functions, after subtracting a Shirely-type background.

Solid-state NMR spectra were recorded using a Bruker Avance III spectrometer equipped with a 14.1 T wide-bore magnet. Powdered samples were packed into 3.2 mm outer diameter ZrO_2 rotors from Bruker and rotated at a magic angle spinning (MAS) rate of 20 kHz. The ^{27}Al MAS NMR spectra were recorded using a short-flip angle pulse (shorter than π/20) with a radiofrequency field strength of ∼100 kHz to ensure that the spectra are quantitative and are the result of averaging 256 transients with a recycle interval of 5 s. The ^{7}Li MAS NMR spectra were recorded using a short-flip angle pulse (shorter than π/12) with a radiofrequency field strength of ∼106 kHz to ensure quantification and are the result of averaging 32 transients with a recycle interval of 10 s. ^{27}Al NMR spectra and ^{7}Li NMR spectra are shown relative to 1.1 M $Al(NO_3)_3$ in D_2O and 1 M LiCl in D_2O, respectively. For the ^{27}Al NMR spectra acquisition, $Al(acac)_3$ (δ_{iso} = 0.0 ppm) was used as a secondary reference.

Scanning transmission electron microscopy (STEM) measurements were performed on an FEI Titan Themis operated at 200 kV, equipped with a CEOS DCOR probe corrector, a SuperX energy dispersive X-ray spectrometer (EDX) and a 4k × 4k Ceta CMOS camera. High-Angle Annular Dark-Field (HAADF) images were acquired with a probe convergence angle of 20 mrad and inner/outer collection angles of 60 and 200 mrad, respectively. Selected area electron diffraction patterns (SADPs) were indexed and fitted using Recipro.[21] Samples for transmission electron microscopy were prepared by dispersion of powder in methyl isobutyl ketone (largely immiscible with water to avoid formation of lithium carbonate) before drop casting onto lacey C/Cu grids purchased from EM Resolutions Ltd, UK.

2.4 Characterisation by thermal and electrical measurements

TGA measurements were performed using a Netzsch STA449 simultaneous thermal analyser. Measurements were made under Ar atmosphere, with a heating rate of 5 °C per minute, and a background correction was applied using a prior baseline run to ensure accuracy of the measurements. The electrical conductivity of the samples was measured in air using a Li-ion blocking Au-electrodes. Au paste was coated on the pellet surface and cured in air at 700 °C for 2 hours. All measurements were made in the temperature range between 25 and 450 °C using an HP 4192A Impedance and Gain Phase Analyser (5 Hz to 13 MHz; 100 mV) interfaced with a PC. A two-probe measurement was used, and prior to each measurement, the samples were equilibrated for about 2–24 h at a constant temperature. All measurements were made during both heating and cooling cycles to check the reproducibility of the data. Dimensions of the garnet samples used for electrical measurements range from 0.11 to 0.15 cm in thickness and 1.2 to 1.32 cm in diameter.

3. Results and discussion

3.1 *Ex situ* powder X-ray diffraction

PXRD patterns of the parent $Li_5La_3M_2O_{12}$ (M = Nb, Ta, Nb/Ta) sintered at 900 °C (I) and at 1100 °C (II) together with the standard pattern $Li_5La_3Nb_2O_{12}$ reported on the Inorganic Crystal Structure Database (ICSD: 18586) are shown in Fig. 1. The PXRD peak positions are the same across the three compositions sintered at both 900 °C and 1100 °C, and all closely match the peak positions of the database reference without major impurity peaks. It is expected that the

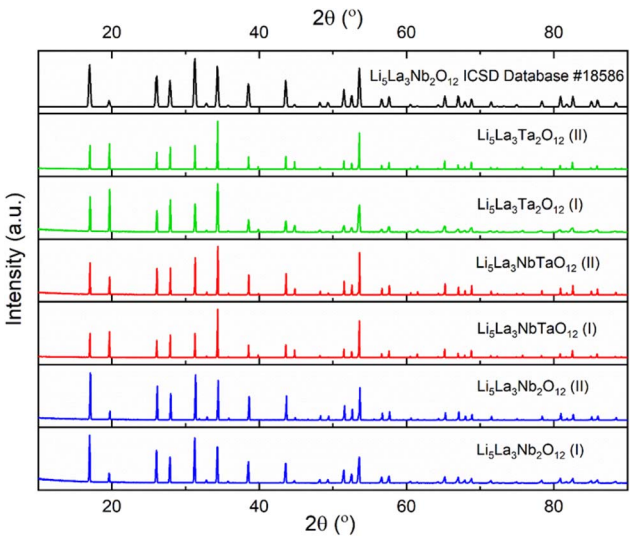

Fig. 1 *Ex situ* PXRD patterns of $Li_5La_3M_2O_{12}$ (M = Nb, Ta, Nb/Ta) prepared at 900 °C (denoted (I)) and at 1100 °C (denoted (II)) for 24 h with a heating and cooling rate of 5 °C per minute, together with the pattern of the inorganic crystal structure database for cubic $Li_5La_3Nb_2O_{12}$ (ICSD #: 18586) for comparison.

compositions with Nb, Ta, and the mixed Nb and Ta on the M-site have the same diffraction patterns as the six coordinate Nb^{5+} and Ta^{5+} have the same ionic radii of 0.64 Å,[22] and each composition should have the same stoichiometric ratios of Li, La, M (Nb and/or Ta) and O. From the PXRD patterns, it can be concluded that at both sintering temperatures all samples form the Li_5-garnet, belonging to the $Ia\bar{3}d$ space group, as the main phase. Fig. S1–S3 (see SI) show the PXRD data for Nb, Ta and Nb/Ta phases synthesis and corresponding precursors compounds.

The unit cell parameters for all samples were found to be 12.73–12.77 Å. These values are comparable to the literature,[5,23] further confirming that cubic garnet structures were synthesised. Additionally, it was observed that the garnets containing Nb showed a slight decrease in lattice parameter at the higher sintering temperature, whereas the Ta only sample showed the same cell parameter at both sintering temperatures. The unit cell of the garnet may decrease due to the formation of small amounts of impurity as a secondary phase, preventing the formation of the garnet in the desired stoichiometric ratio or if a material decomposes at elevated temperatures, in turn changing the structure. However, the observed changes in the unit cell parameter are found to be rather small value, and therefore, the proposed compositional changes are only speculative, requiring further investigation.

3.2 *In situ* powder X-ray diffraction

A series of *in situ* PXRD experiments during solid-state synthesis was performed to clarify the influence of different parameters on the synthesis process. Interesting factors to consider were the variations in the number of intermediate annealing temperatures, their timing, and heating rates. As we used the laboratory PXRD for *in situ* measurements, the heating rates were mostly determined by the number of intermediate annealing temperatures, because the measurements took 30 minutes at each temperature step. Therefore, through careful experimental design, a series of multiple heating steps enabled the solid-state transformation to be followed in detail, thus helping to understand the solid state reaction mechanism that occurs between 700 °C and 1100 °C, and the necessity of the high temperatures during this synthesis.

Investigation of the phase formation of $Li_5La_3Nb_2O_{12}$ began using the mixture, which had been pre-annealed *ex situ* in the laboratory oven for 10 hours at 750 °C. Therefore, in the starting powder at room temperature (RT), a small amount of the targeted phase $Li_5La_3Nb_2O_{12}$ was present. Thus, even if considerable amounts of $Li_5La_3Nb_2O_{12}$ had formed during the *ex situ* pre-annealing step at 750 °C, it was largely decomposed to La_2LiNbO_6 (84 wt%) and Li_3NbO_4 (9 wt%) on cooling back to RT. The marginally small amount of targeted phase $Li_5La_3Nb_2O_{12}$ (4 wt%) as well as minor impurities La_2O_3 (1 wt%) of non-reacted high-temperature decomposition phase of $La(OH)_3$ and La_3NbO_7 (2 wt%, probably formed at 750 °C during *ex situ* pre-annealing and preserved during cooling to RT) were also observed in the starting pre-annealed *ex situ* material.

It is observed that the *ex situ* pre-annealed at 750 °C mixture quickly transforms before 700 °C (Fig. 2), giving 54 wt% of the targeted $Li_5La_3Nb_2O_{12}$ phase at 700 °C, while undesirable La_2LiNbO_6 completely disappears by 800 °C *via* decomposition to La_2O_3 and other possible amorphous phases. The target phase $Li_5La_3Nb_2O_{12}$ reaches 88 wt% at 1075 °C before unexpected complete decomposition into La_2LiNbO_6 and Li_3NbO_4 after

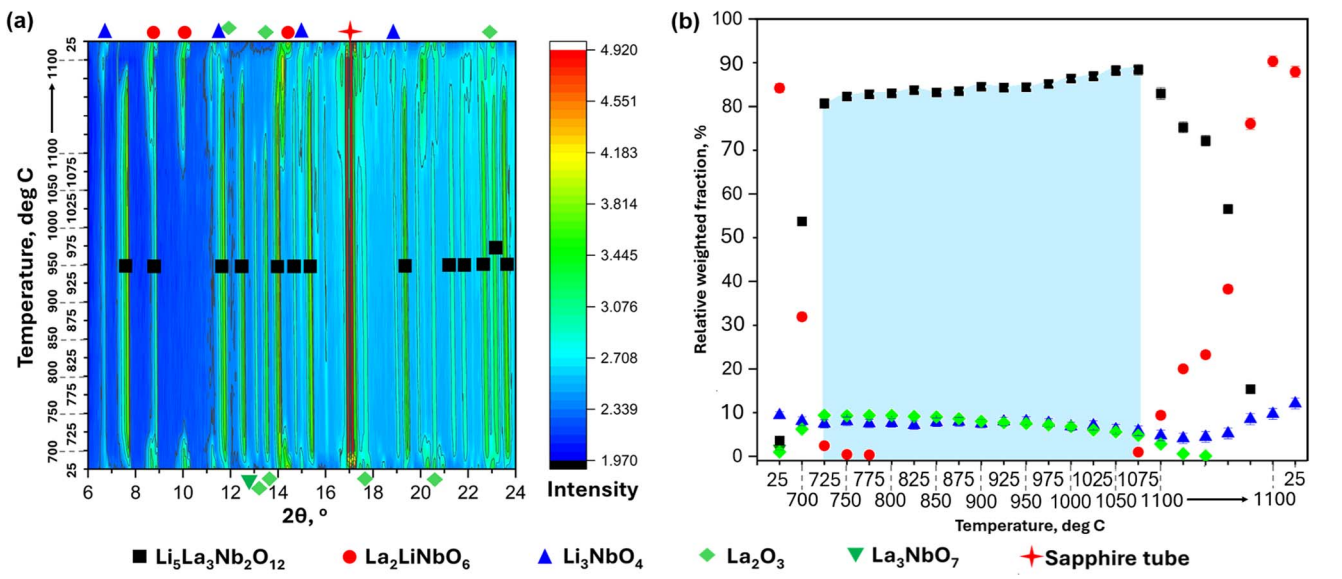

Fig. 2 (a) 2D contour plot (logarithmic scale of intensities) for *in situ* PXRD during synthesis of $Li_5La_3Nb_2O_{12}$ *via* slow heating of pre-annealed at 750 °C sample (heating rate 20 °C min^{-1}, 30 min per each scan); diffraction patterns were recorded during heating (25–1100 °C), isothermal at 1100 °C, and at 25 °C after cooling. Selected peaks are represented by the corresponding symbols as shown. (b) Weighted fractions of crystalline phases (determined by Rietveld refinement) during *in situ* PXRD during synthesis of $Li_5La_3Nb_2O_{12}$ *via* slow heating of pre-annealed at 750 °C sample. The error bar of relative weighted fraction is smaller than the size of the symbol when not shown. The light blue shaded area is a guide to the eye to visualise the temperature range under which highest yield of the target phase was obtained.

1075 °C. Although the very little impurity of La_3NbO_7 was formed during the pre-annealing step, it reacted with other phases before reheating during *in situ* PXRD to 700 °C. These results allow us to speculate that using a very high temperature of 1100 °C for the synthesis of $Li_5La_3Nb_2O_{12}$ may not be necessary, and extended annealing at a lower temperature can be preferable and more convenient.

Although the maximal amount of $Li_5La_3Nb_2O_{12}$ obtained during *in situ* PXRD experiment was 88 wt%, it is possible that the slightly different conditions, which are necessary for *in situ* measurement prevented 100 wt% transformation. During *ex situ* synthesis, the powder is pressed and a larger volume of the powder is used, while during *in situ* PXRD synthesis the powder was loose and a small amount of powder (cylinder of dia. 1 mm and of length 10 mm) was used. This scaling down of the material during synthesis may have prevented the full transformation because part of the powder may have stuck to the capillary tube walls and, therefore, was not involved in the reaction. To further understand whether the multiple annealing steps between 700 °C and 1100 °C (during which PXRD data were recorded) had a substantial influence on the transformation behaviour, the pre-annealed *ex situ* at 750 °C mixture was used for a different temperature profile: heating from RT to 700 °C for a short time to record one diffraction data at this temperature and subsequent heating up to 1100 °C and holding at that temperature for 4 hours while continuously recording diffraction data (Fig. 3).

The room-temperature results for the freshly made *ex situ* pre-annealed mixture were almost identical to the previous mixture (Fig. 2 and 3), demonstrating 88 wt% of La_2LiNbO_6 and 8 wt% of Li_3NbO_4 with only 4 wt% of the targeted phase $Li_5La_3Nb_2O_{12}$. The first data point at 700 °C indicated that the transformation proceeded in the identical way to the previous experiment, with the targeted phase $Li_5La_3Nb_2O_{12}$ reaching 48 wt%. After that, the mixture was fast heated up to 1100 °C and measured at this temperature during hold. Very unexpected results indicate 91 wt% of targeted phase $Li_5La_3Nb_2O_{12}$ within 1 hour after reaching 1100 °C and subsequent complete decomposition of $Li_5La_3Nb_2O_{12}$ by the end of 3 hours hold at 1100 °C. The decomposition products were La_2LiNbO_6 (87 wt%) and Li_3NbO_4 (13 wt%), *i.e.* the same mixture was formed *in situ* after 3 hours hold at 1100 °C, as the starting mixture after *ex situ* pre-annealing at 750 °C. Using such a pre-annealed mixture allowed to synthesise the almost pure targeted phase $Li_5La_3Nb_2O_{12}$ (with restrictions imposed by scaling down the reaction for the *in situ* PXRD experiment). To check whether this mixture can again produce the targeted phase $Li_5La_3Nb_2O_{12}$, a second heating profile was used for *in situ* PXRD measurements (Fig. 3). Despite the same temperature profile for the second cycle, only decomposition products La_2LiNbO_6 and Li_3NbO_4 were observed without any variation in their amount. Attempt was made to synthesise the targeted phase $Li_5La_3Nb_2O_{12}$ during *in situ* PXRD measurements without an *ex situ* pre-annealing step at 750 °C in an ordinary laboratory oven. Two different experiments were performed with: (i) only 2 annealing steps (700 °C and 1100 °C) to simulate the standard *ex situ* synthesis process (Fig. 4) and (ii) multiple intermediate temperature steps to clarify the fine details of the solid-state synthesis process (Fig. 5).

In situ PXRD measurements of as-prepared mixture (Fig. 4) contained at RT the mixture of starting materials Nb_2O_5, Li_2CO_3, $La(OH)_3$ (formed during preparation of the initial mixture from the correctly weighted La_2O_3 *via* hydration in air).

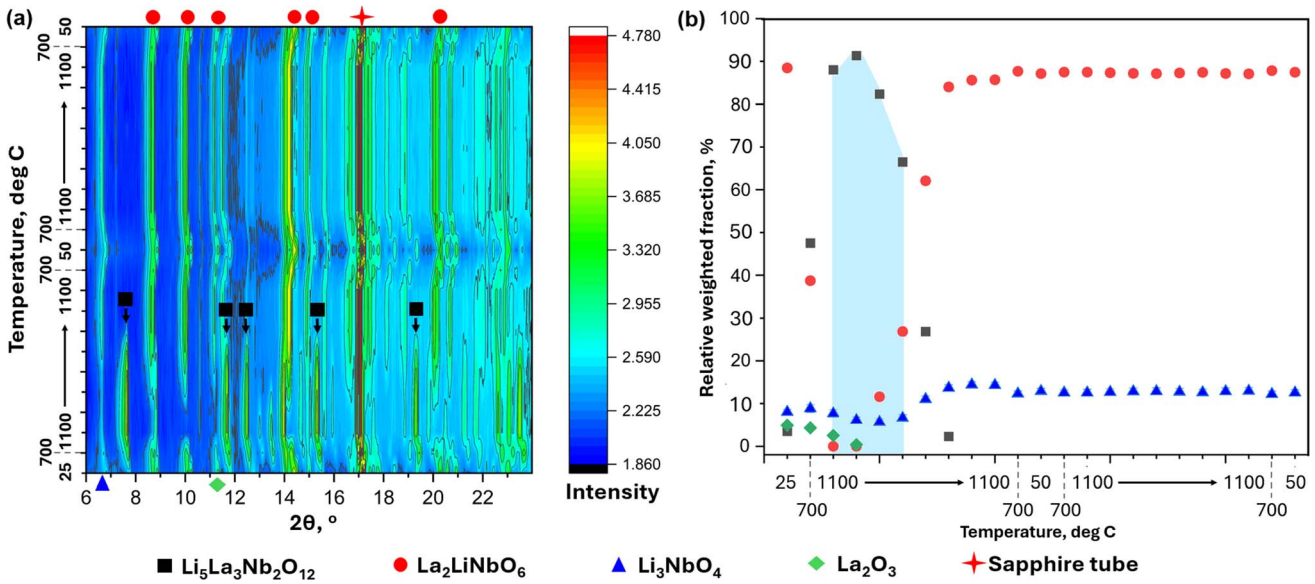

Fig. 3 (a) 2D contour plot (logarithmic scale of intensities) for *in situ* PXRD during synthesis of $Li_5La_3Nb_2O_{12}$ *via* heating to different temperatures and holding at 1100 °C for a prolonged time (heating rate 20 °C min^{-1}, 30 min per each scan); two heating, isothermal at 1100 °C for 4 hours, and cooling cycles are shown. Selected peaks are represented by the corresponding symbols as shown. (b) Weighted fractions of crystalline phases (determined by Rietveld refinement) during *in situ* PXRD during synthesis of $Li_5La_3Nb_2O_{12}$ *via* heating to different temperatures and holding at 1100 °C for 4 hours. The error bar of relative weighted fraction is smaller than the size of the symbol when not shown. The light blue shaded area is a guide to the eye to visualise the temperature range under which highest yield of the target phase was obtained.

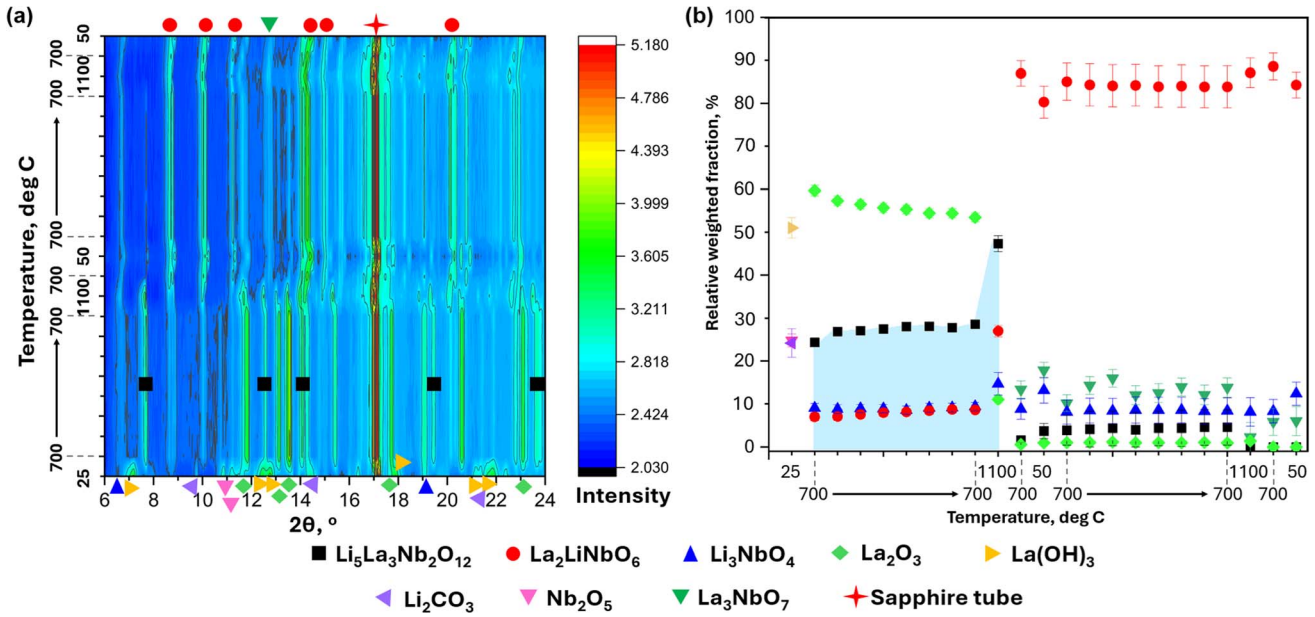

Fig. 4 (a) 2D contour plot (logarithmic scale of intensities) for *in situ* PXRD during synthesis of $Li_5La_3Nb_2O_{12}$ *via* heating to different temperatures and holding at 700 °C for 3.5 hours (heating rate 20 °C min, 30 min per each scan); two heating and cooling cycles are shown. Selected peaks are represented by the corresponding symbols (the same symbols as those for the corresponding relative weighted fractions). (b) Weighted fractions of crystalline phases (determined by Rietveld refinement) during *in situ* PXRD during synthesis of $Li_5La_3Nb_2O_{12}$ *via* heating to different temperatures and holding at 700 °C for 3.5 hours. The error bar of the relative weighted fraction is smaller than the size of the symbol when not shown. The light blue shaded area is a guide to the eye to visualise the temperature range under which highest yield of the target phase was obtained.

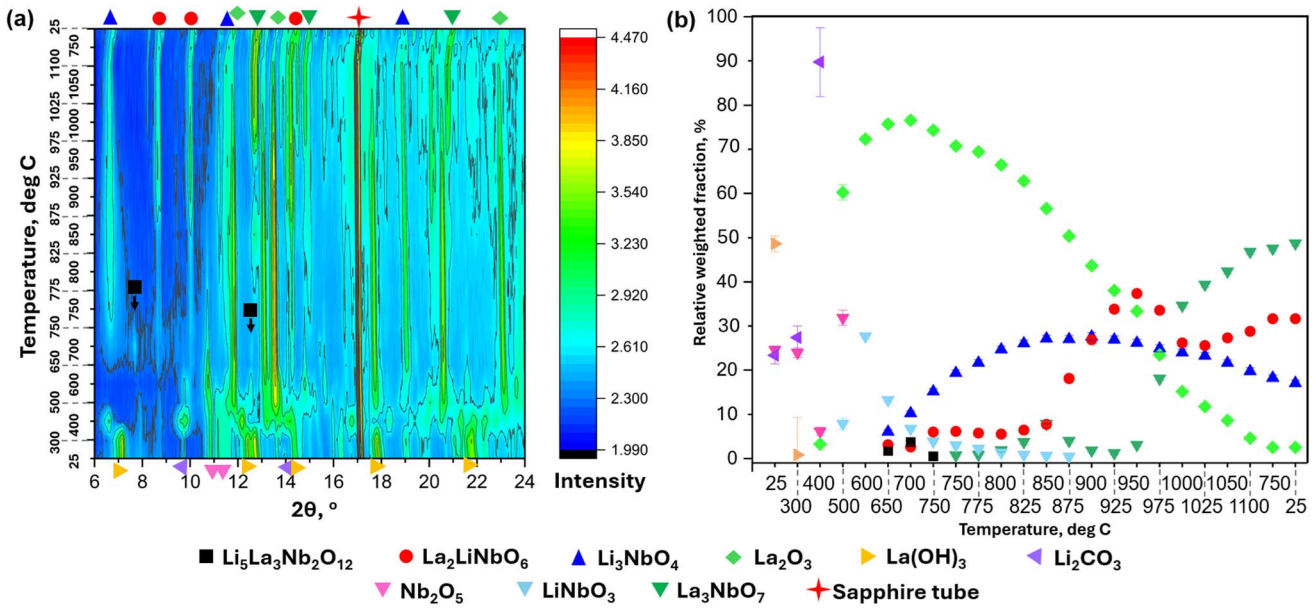

Fig. 5 (a) 2D contour plot (logarithmic scale of intensities) for *in situ* PXRD during synthesis of $Li_5La_3Nb_2O_{12}$ *via* slow heating (heating rate 20 °C min^{-1}, 30 min per each scan); diffraction patterns were recorded during heating (25–1100 °C) and at 750 °C and 25 °C during cooling. Selected peaks are represented by the corresponding symbols, as shown. (b) Weighted fractions of crystalline phases (determined by Rietveld refinement) during *in situ* PXRD during synthesis of $Li_5La_3Nb_2O_{12}$ *via* slow heating. The error bar of relative weighted fraction is smaller than the size of the symbol when not shown.

Fast heating up to 700 °C indicated the fast formation of the targeted phase $Li_5La_3Nb_2O_{12}$ (25 wt%) with impurities La_2LiNbO_6 (7 wt%) and Li_3NbO_4 (9 wt%) and unreacted La_2O_3 (60 wt%). Subsequent annealing at 700 °C for 3.5 h had a minor impact on these formed phases. Ramping the temperature to 1100 °C allowed to increase the concentration of the targeted

$Li_5La_3Nb_2O_{12}$ to 47%. Previous experiments (Fig. 2 and 3) demonstrated that longer annealing at 1100 °C would result in the complete decomposition of $Li_5La_3Nb_2O_{12}$, hence, the mixture was cooled to RT through one intermediate short temperature step at 700 °C to record one diffraction pattern. *In situ* diffraction data indicate almost complete decomposition of the targeted phase already on cooling to 700 °C (Fig. 4), which perfectly correlates with results from *ex situ* pre-annealing (first RT results on Fig. 2 and 3). Second identical heating cycle (Fig. 4) was performed for *in situ* PXRD with the same temperature profile, but the results indicated that the more stable phase of La_2LiNbO_6 does not participate in the reaction, and its amount remained almost unchanged during the second heating cycle. The amount of the targeted phase $Li_5La_3Nb_2O_{12}$ slightly increased during the second heating cycle to 5 wt%, but the complete decomposition of this phase was observed on the second heating to 1100 °C.

There is an acceptable correlation between completely *in situ* synthesis during PXRD measurements (Fig. 4) and *in situ* synthesis with *ex situ* pre-annealing step at 750 °C. The formation and decomposition of the targeted phase $Li_5La_3Nb_2O_{12}$ at 700 °C and the irreversible decomposition of the targeted phase $Li_5La_3Nb_2O_{12}$ during the second heating cycle, and similar decomposition phases and intermediate phase during all heat treatments were observed. The interesting observation is the possibility to synthesise the almost pure targeted phase $Li_5La_3Nb_2O_{12}$ from the mixture of La_2LiNbO_6 and Li_3NbO_4 after an *ex situ* pre-annealing step at 750 °C (Fig. 2 and 3), while using the same mixture after heating it up to 750 °C makes synthesis of the targeted $Li_5La_3Nb_2O_{12}$ phase impossible (Fig. 3 and 4).

To clarify the fine details of the solid-state synthesis process, the as-prepared mixture was used for *in situ* synthesis during PXRD measurements with multiple temperature steps (Fig. 5). As expected, the initial as-prepared mixture at RT (Fig. 5) contained the starting materials Nb_2O_5, Li_2CO_3, $La(OH)_3$ (formed during preparation from La_2O_3). The diffraction peaks from a crystalline Nb_2O_5 disappear after 500 °C. The formation of $LiNbO_3$ can be assigned to the reaction between Nb_2O_5 and Li_2CO_3 around 500 °C. At 650 °C, the transformation of $LiNbO_3$ into Li_3NbO_4 is observed; this transformation was previously observed during the synthesis of lithium niobates doped by transition metal.[24] An important observation is a substantial amorphisation of the starting materials (Li_2CO_3, $La(OH)_3$, Nb_2O_5) around 400 °C: all diffraction peaks at this temperature are very broad; $La(OH)_3$ is undergoing the transformation to crystalline La_2O_3 *via* a substantially amorphous intermediate state (Fig. 5). At 500 °C, the highly crystalline La_2O_3 and $LiNbO_3$ with low-crystalline Nb_2O_5 are observed. Subsequent heating up leads to decreasing the amount of $LiNbO_3$ at 650 °C (with subsequent disappearance after heating to 875 °C), formation of Li_3NbO_4, La_2LiNbO_6, and $Li_5La_3Nb_2O_{12}$. The targeted $Li_5La_3Nb_2O_{12}$ is formed only within a temperature range 650–750 °C. During this slow heating process, the amount of this phase remains very small due to the competitive formation of more stable Li_3NbO_4 and La_2LiNbO_6 phases. Thus, the very slow heating *via* multiple annealing temperature steps, to record the diffraction patterns at each temperature, changed the synthesis conditions considerably and prevent the detailed analysis of the synthesis process by *in situ* PXRD. It is important to underline that no quantifiable amount of $LaAlO_3$ was observed during *in situ* PXRD experiments.

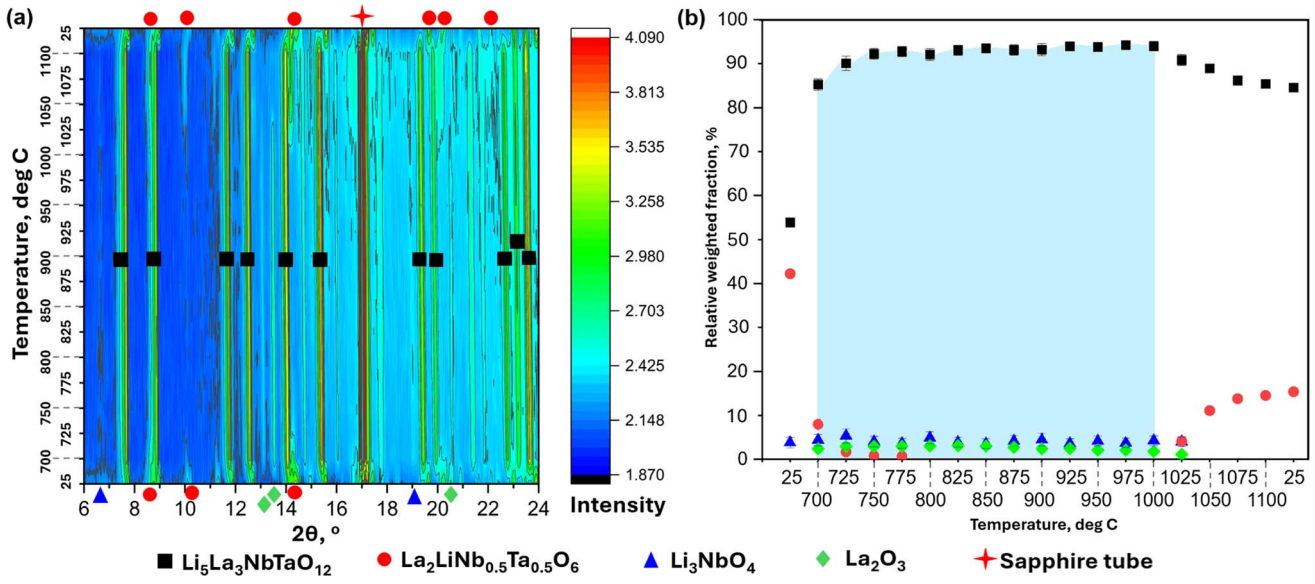

Fig. 6 (a) 2D contour plot (logarithmic scale of intensities) for *in situ* PXRD during synthesis of $Li_5La_3NbTaO_{12}$ *via* slow heating of pre-annealed at 750 °C sample (heating rate 20 °C min^{-1}, 30 min per each scan); diffraction patterns were recorded during heating (25–1100 °C) and at 25 °C after cooling. Selected peaks are represented by the corresponding symbols, as shown. (b) Weighted fractions of crystalline phases (determined by Rietveld refinement) during *in situ* PXRD during synthesis of $Li_5La_3NbTaO_{12}$ *via* slow heating of pre-annealed at 750 °C sample. The error bar of relative weighted fraction is smaller than the size of the symbol when not shown. The light blue shaded area is a guide to the eye to visualise the temperature range under which highest yield of the target phase was obtained.

To analyse the possible influence of the Ta substitution, additional *in situ* PXRD measurements were performed during synthesis of $Li_5La_3NbTaO_{12}$ (Fig. 6). The initial mixture was pre-annealed *ex situ* in the laboratory oven for 10 hours at 750 °C, and the resulting powder at RT showed a significant amount of targeted phase $Li_5La_3NbTaO_{12}$ (54 wt%) in contrast to all *ex situ* pre-annealed experiments for synthesis of $Li_5La_3Nb_2O_{12}$ (Fig. 2 and 3). Subsequent heating to 700 °C during *in situ* PXRD measurements allowed for an increase in the amount of targeted phase to 85 wt%, and further heating allowed achieving an almost pure sample with 94 wt% of targeted $Li_5La_3NbTaO_{12}$ at 975 °C. Further heating up resulted in the partial decomposition into more stable $La_2LiNb_{0.5}Ta_{0.5}O_6$ and other possible amorphous phases. $Li_5La_3NbTaO_{12}$ and $La_2LiNb_{0.5}Ta_{0.5}O_6$ were observed by *in situ* PXRD as crystalline phases at 1050 °C and above, as well as during subsequent cooling to RT. Still, a substantial amount of the targeted $Li_5La_3NbTaO_{12}$ (85 wt%) was observed at RT at the end of the *in situ* synthesis (Fig. 6), which contradicts the results for the targeted phase $Li_5La_3Nb_2O_{12}$ (Fig. 2–4).

3.3 Raman spectroscopy

The phase of the synthesised garnets can be further explored using Raman spectroscopy, displayed in Fig. 7. Raman spectra can be split into three regions: (i) low-energy region below about 300 cm^{-1}, (ii) intermediate-energy region between 300 and 550 cm^{-1} and (iii) a high-energy region above 550 cm^{-1}.[25] The high-energy region shows the vibrational stretching modes of the octahedral units, here the peak at 720 cm^{-1} and 738 cm^{-1} are assigned to Nb and Ta, respectively. The broad intermediate region consists of vibrational bending modes of octahedral and tetrahedral Li, and finally the low-energy region is assigned to the La translational stretching modes.[25] In addition to the garnet peaks, a high energy peak is observed at around 1075 cm^{-1}, which is characteristic of a carbonate vibrational stretching mode, indicating the presence of surface layer lithium carbonate contamination on a sample.

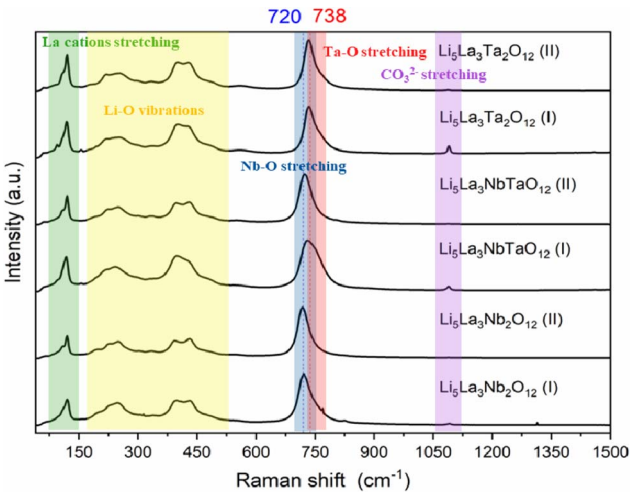

Fig. 7 Room temperature Raman spectra from the surface of $Li_5La_3M_2O_{12}$ (M = Nb, Ta, Nb/Ta) pellet, sintered at either 900 °C (I) or 1100 °C (II). Spectra are obtained from an average of 20 points measured randomly across the surface.

The Raman spectra further confirm formation of a cubic garnet structure across both sintering temperatures for each composition. This is evidenced by the presence of broad, characteristic peaks associated with the garnet structure.[25] Additionally, due to Raman spectroscopy's sensitivity to local bonding environments, subtle variations in M-site coordination can be resolved, allowing differentiation between Nb and Ta samples. The spectra indicate the successful formation of a mixed M-site garnet, which is not easily distinguishable by PXRD. It should be noted that for all compositions after sintering at 1100 °C, a shoulder peak emerges at 110 cm^{-1}, indicating the existence of small amounts of lower symmetry tetragonal phase.

3.4 Scanning electron microscopy

Microstructure and surface topography were investigated using scanning electron microscopy (SEM). The set of back scattered electron (BSE) images of the top pellet surfaces for each $Li_5La_3M_2O_{12}$ (M = Nb, Ta, Nb/Ta) garnet synthesised at both 900 °C and 1100 °C (Fig. 8) show the difference in microstructure across the samples. Across all compositions, samples exhibit a homogeneous microstructure with poorer densification observed when sintered at 900 °C compared to those sintered at 1100 °C, this effect is most prominent in $Li_5La_3NbTaO_{12}$ (Fig. 8b and e). Given that all samples were subjected to the same dwell time, the observed differences in grain size and density could be attributed to the higher thermal energy at 1100 °C, which enhances atomic mobility and promotes particle growth. Densification strongly influences the ionic conductivity of the material, as lower density and higher porosity materials typically result in reduced conductivity due to the presence of greater grain boundary resistance.[26] Furthermore, in the context of lithium metal battery applications, a porous solid electrolyte contains voids which can accelerate dendrite formation, compromising performance.[27] Therefore, the SEM analysis demonstrates that higher sintering temperatures lead to improved densification and grain growth, which are expected to enhance the ionic conductivity and electrochemical stability of the material. Additionally, the BSE imaging clearly reveals contrast associated with secondary surface contamination, namely Li_2CO_3 since carbon is found in EDS analysis (Fig. S4–S6, see SI). From the EDS mapping, it is apparent that all the elements are distributed evenly in the particles. Heat treatment of the pellets in Ar atmosphere is proven to be effective in removing surface contamination, which is crucial to subsequent steps, especially for lithium melting when preparing either full or symmetrical cells, since lithium carbonate renders the garnet surface highly lithiophobic.[28] The back scattered electron images of the pellets after removal of the lithium carbonate are shown in Fig. S7 (see SI).

3.5 Transmission electron microscopy

To assess the ordering over nanometric length scales, scanning transmission electron microscopy (STEM), was performed on

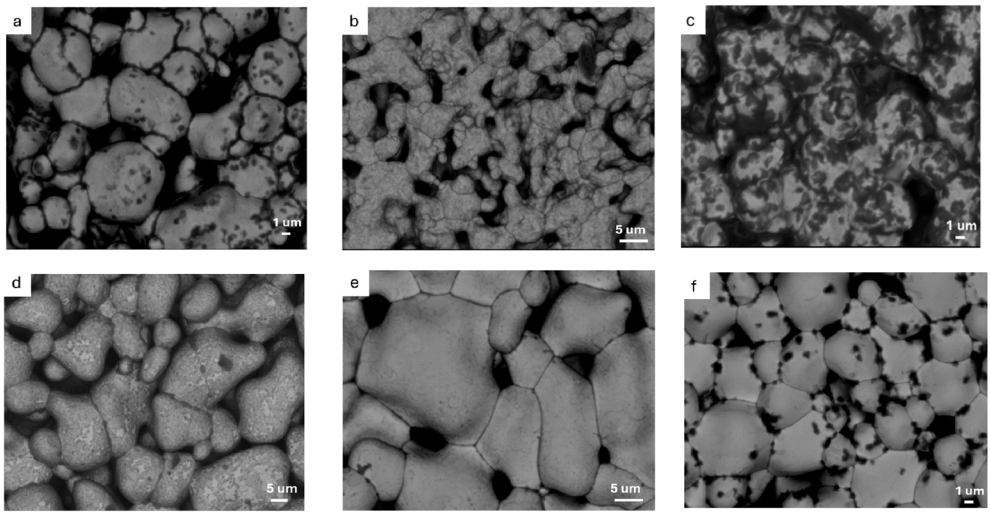

Fig. 8 Backscattered electron detector (BSED) SEM images of the top surface of garnet pellets sintered at 900 °C (a) $Li_5La_3Nb_2O_{12}$, (b) $Li_5La_3NbTaO_{12}$, and (c) $Li_5La_3Ta_2O_{12}$ and at 1100 °C (d) $Li_5La_3Nb_2O_{12}$, (e) $Li_5La_3NbTaO_{12}$, and (f) $Li_5La_3Ta_2O_{12}$. The dark spots on the garnet surface are lithium carbonate.

a subset of samples. Fig. 9(a–c) show atomic resolution high angle annular dark field (HAADF) images and Fig. 9(d–f) the corresponding selected area electron diffraction patterns (SADPs) data from samples $Li_5La_3Nb_2O_{12}$, $Li_5La_3Ta_2O_{12}$ and $Li_5La_3NbTaO_{12}$, respectively. Data obtained from the ⟨001⟩-type zone axes, a high degree of local ordering can be seen, with all samples exhibiting the typical garnet-like ordering,[29] with a central La cation surrounded by four Nb/Ta cations, as depicted in the inset of Fig. 9(c). Based on measurements of the *d*-spacings, all samples exhibit an essentially cubic structure, although the measurements suggest a very slight tetragonality, with an *a*/*b* ratio (based on the nominal *hkl* indexing) of ~1.01, consistent with the high symmetry observed by PXRD. Selected area electron diffraction data confirmed the absence of any superstructure reflection in all samples and no diffuse scattering, indicating a lack of any short-range ordering in all investigated samples.

3.6 X-ray photoelectron spectroscopy

X-ray photoelectron spectroscopy (XPS) analysis on the sample pellets sintered at 1100 °C and allowed to cool to room tempertaure (RT) confirmed the presence of the expected elements in each sample, as summarised in Table 1 and Fig. S8, see SI. The binding energies observed for each element are consistent across the three compositions, indicating similar chemical environments. For all garnets, the La $3d_{5/2}$ core level peak is fitted with a single component at 833.0 eV (FWHM 2.23 eV) and exhibits the shake-up feature typical of La(III). Although on the lower binding energy side of the typical range for La(III), 833.8–835.2 eV,[30] La(III) in a mixed metals oxide matrix shows lower

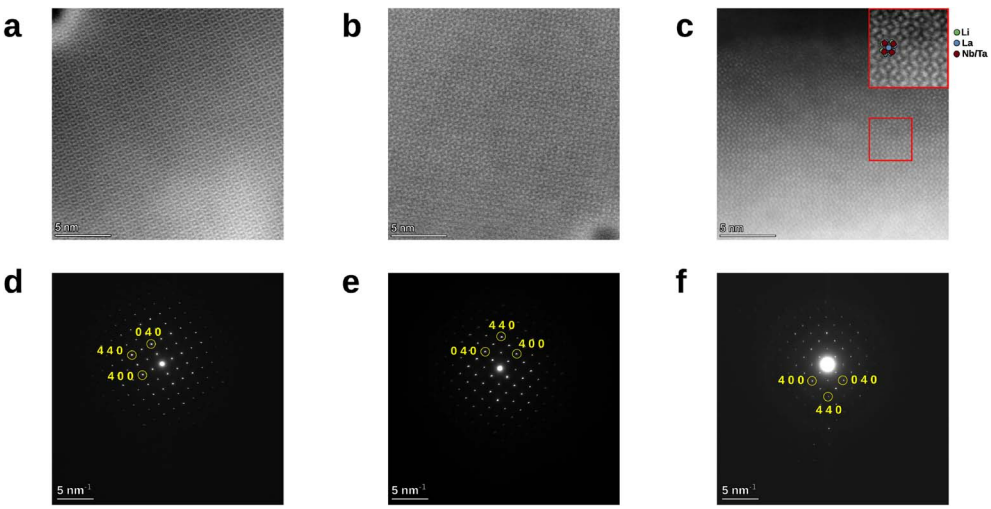

Fig. 9 Scanning transmission electron microscopy data from $Li_5La_3Nb_2O_{12}$, $Li_5La_3Ta_2O_{12}$ and $Li_5La_3NbTaO_{12}$ samples showing (a–c) atomic resolution HAADF images and (d–f) SADPs, respectively. Both HAADF and SADPs were acquired from the ⟨001⟩-type zone axes of grains.

Table 1 XPS binding energies (BE) and atomic surface concentration (ASC) % for the surface of $Li_5La_3M_2O_{12}$ (M = Nb, Ta, Nb/Ta) pellets sintered at 1100 °C, measured at room temperature. BE values ± 0.1 eV

Element and orbital	$Li_5La_3Nb_2O_{12}$		$Li_5La_3NbTaO_{12}$		$Li_5La_3Ta_2O_{12}$	
	BE (eV)	ASC (%)	BE (eV)	ASC (%)	BE (eV)	ASC (%)
La $3d_{5/2}$	833.0	1.3	832.9	0.4	833.1	0.9
O 1s	531.7	47.8	531.8	49.9	531.7	45.3
	528.7	7.1	528.7	3	529.0	6.9
Nb $3p_{3/2}$	363.7	0.8	363.8	0.2	—	—
C 1s	289.9	15.7	289.9	18.3	290.0	18.3
	285.0	2.7	285.0	2.5	285.0	2.5
Ta $4d_{5/2}$	—	—	228.5	0.3	228.7	0.8
Li 1s	55.0	24.7	55.1	25.4	55.0	27.6

values of the binding energy,[31] this is also confirmed by a Δ*j* *ca.* 16.7 eV and the position of the satellite peak at 837.3 eV, giving a multiplet separation of *ca.* 4.3 eV from the parent peak, close to the expected value for pure La(III) oxide, La_2O_3, (4.9 ± 0.2) eV.[32] In the Ta-containing garnet, the Ta $4d_{5/2}$ core level peak is fitted with a single component at 228.7 eV (FWHM 3.6 eV) and shows a single chemical environment, within the expected range for Ta(V).[28] In the Nb-containing garnet, the Nb $3p_{3/2}$ core level peak is fitted with a single component at 363.7 eV (FWHM 2.7 eV), and shows a single chemical environment, within the expected range for Nb(V).[31,33] This is preferred to the more intense 3d transition because it overlaps with La $4p_{1/2}$. Similar fitting parameters were used to model the Nb $3p_{3/2}$ and Ta $4d_{5/2}$ core level peaks in the garnet containing both Nb and Ta, obtaining consistent results.

When comparing the M-site elements (Nb and/or Ta), differences in both binding energy and atomic percentage are observed for the mixed composition *vs.* both the single substituted samples. In the pure Nb and Ta samples, the M-site elements are present at approximately 0.8 atomic %, whereas the mixed composition shows a lower value of 0.5 atomic %. This may indicate a reduced amount of the garnet phase exposed at the surface in the mixed sample, likely due a thicker layer of lithium carbonate. Interestingly, the mixed M-site sample also exhibits slightly lower binding energies for both Nb and Ta compared to the single-substitution samples. This could indicate that Nb and Ta may reside in a more electron-rich environment within the mixed-phase garnet, potentially due to modified local bonding environments or variations in oxygen coordination. However, the observed binding energy shifts of 0.1 eV for Nb and 0.2 eV for Ta, are relatively small, suggesting that these changes are not significant, and perhaps just within the experimental error.

The O 1s core level peaks show a profile which is best fitted with two components (FWHM *ca.* 1.7 eV): the higher BE component, *ca.* 531.7 eV, is assigned to oxygen belonging to the carbonate anion, whereas the lower BE component, *ca.* 529 eV, is assigned to the garnets lattice oxygen.[34] The C 1s core level region is fitted with two components: the higher BE component, *ca.* 289.9 eV (FWHM *ca.* 1.2 eV), is assigned to carbon belonging to the carbonate anion, whereas the lower BE component, 285 eV (FWHM *ca.* 1.6 eV), is assigned to adventitious carbon,[35] and used as internal reference for the BE scale. For all the investigated garnets, the Li 1s core level peak is fitted with a single component with maximum at 55.0 eV (FWHM *ca.* 1.5 eV) and assigned to the presence of Li(I).[30,31] Overall, the presence of the garnet phase elements is confirmed, however, the measured atomic concentrations deviate from those expected for a bulk stoichiometric garnet phase, particularly showing an excess of lithium, carbon and oxygen. Since XPS is a highly surface-sensitive technique, probing in the range of about 30 nanometres, it is particularly susceptible to detecting surface composition. The presence of excess Li, C and O, suggests that the garnets' surfaces are coated in a layer of Li_2CO_3 which is likely due to surface reaction of the exposed Li with atmospheric H_2O and CO_2.

3.7 Solid-state NMR spectroscopy

Solid-state NMR spectroscopy of lithium in the 1100 °C base pellets provides a detailed insight into the local chemical environment of lithium ions within the garnet material. Fig. 10 presents the ^{7}Li MAS NMR spectra of $Li_5La_3M_2O_{12}$ (M = Nb, Ta, Nb/Ta), which display a single, well-defined resonance peak at ~1 ppm. Cubic garnets are known to exhibit partial lithium disorder, where lithium ions are distributed across both tetrahedral and octahedral sites (Fig. 10b and c).[6,36] Due to the similar local environments of these sites and rapid lithium-ion hopping at room temperature, the ^{7}Li MAS NMR spectra for it typically yield a single, averaged resonance.[37] A small shoulder at ~0 ppm, that is more pronounced in the Nb-containing samples, can be assigned to the presence of minor amounts of Li_2CO_3 that is consistent with its formation on the surface of the material.

3.8 AC impedance analysis

Typical impedance plots for the parent compound $Li_5La_3Nb_2O_{12}$ obtained at 55 and 100 °C in air, from samples prepared at two sintering temperatures, are shown in Fig. 11. Only pellets that were not in contact with the crucible during sintering were selected for ionic conductivity measurements, to eliminate the influence of undesirable reactions and garnet decomposition on the ionic conductivity. The 55 °C impedance plot for the $Li_5La_3Nb_2O_{12}$ sample sintered at 1100 °C features a large bulk (grain interior, R_b) resistance at the high-frequency region, alongside a grain boundary (R_{gb}) contribution and a tail at low

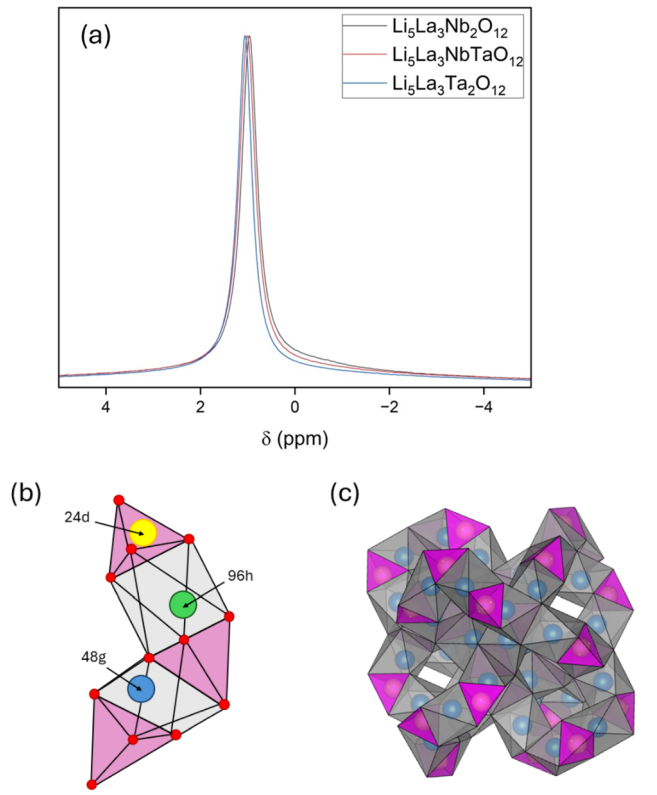

Fig. 10 (a) ^{7}Li (14.1 T, 20 kHz MAS) MAS NMR spectra of powder $Li_5La_3M_2O_{12}$ (M = Nb, Ta, Nb/Ta). (b) Tetrahedral and octahedral frameworks of oxygen (represented as red spheres at the polyhedral corners), which host Li atoms at specific sites: yellow (24 d, tetrahedral), blue (48 g, octahedral), and green (96 h, off-centre octahedral). (c) Illustrates the 3D network of connected oxygen polyhedron accommodating Li atoms (yellow and blue spheres).

frequencies (Fig. 11(c)). In contrast, the sample sintered at 900 °C exhibits primarily a single semicircle in the high-frequency region with a low-frequency tail. When ionically blocking electrodes are employed, the low-frequency tail on the AC impedance plots is characteristic of an ionically conductive material.[26] At temperatures (above ~70 °C), the impedance response for all samples (Fig. 11, S9 and S10, see SI) becomes less distinguishable into separate contributions of bulk, and grain boundary contributions. Therefore, for comparative purposes, the total resistance (combining both bulk and grain boundary contributions) is used to represent the overall electrical conductivity across the full temperature range studied.

The resistance derived from the Nyquist plot at low-frequency intercept to the real axis, the thickness of the pellet, l, and the surface area of the electrode, A, were used to calculate the ionic conductivity, σ, of the investigated three garnet-type samples:

$$\sigma = \frac{l}{RA} \quad (1)$$

The activation energy for the lithium conductivity is calculated by fitting the data to the Arrhenius equation:

$$\log_{10}\sigma_{ion}T = \log_{10}A - \frac{E_a}{2.303\,kT} \quad (2)$$

where A is the pre-exponential factor, k is the Boltzmann constant and T is the absolute temperature. The temperature-dependent pre-exponential factor of the garnet-type electrolyte takes the concentration, diffusion coefficient and entropy into consideration. Here, this was taken directly from the literature and was not calculated for these samples, as it has been assumed that the structures have the ideal stoichiometric concentration of lithium.

Lithium-ion conductivity of the parent garnets $Li_5La_3M_2O_{12}$ (M = Nb, Ta, Nb/Ta) can be obtained *via* Arrhenius plots. Fig. 12 presents the Arrhenius behaviour of $Li_5La_3Nb_2O_{12}$ sintered at both 900 °C and 1100 °C. The conductivity data, collected during both heating and cooling cycles, follow a linear trend (dashed lines in the plots), indicating that the measurements reflect equilibrium behaviour. The overall trends align well with those reported in literature for similar materials. The $Li_5La_3Nb_2O_{12}$ sample prepared in 2006 by Thangadurai *et al.* sintered at 1000 °C lies between the two sintering conditions used in this study, offering a useful point of comparison.[38] In general, the Nb- and Ta-only samples show higher conductivities when sintered at 900 °C compared to 1100 °C. Conversely, the mixed Nb/Ta sample displays improved conductivity when sintered at 1100 °C. These results highlight the intricate balance between phase purity and microstructure. While higher sintering temperatures promote densification, which should enhance ionic transport, in this study they also generate impurity phases, which can reside particularly at grain boundaries, increasing resistance and thus reducing overall conductivity. The samples sintered at 900 °C all exhibit comparable conductivities, as expected for samples with similar phase composition and fewer impurities. However, the 1100 °C samples show a broader range of conductivity values, indicating varying responses to high-temperature processing. The highest conductivity at 55 °C was observed for the $Li_5La_3NbTaO_{12}$ composition sintered at 1100 °C, with a value of 4.8×10^{-5} S cm^{-1}. Above 300 °C, the conductivities of all samples converge, this high-temperature effect is beyond the scope of the present study, and the analysis focuses on the Arrhenius behaviour between 25 °C and 200 °C.

From the Arrhenius plot, the activation energies for lithium-ion conduction were extracted (Table 2).[5,23,38–44] All samples sintered at 900 °C have activation energies of 0.50 eV or lower, reflecting favourable lithium-ion mobility. However, the Ta-substituted sample sintered at 1100 °C exhibits a significantly higher activation energy of 0.62 eV, highlighting a difference in the sample compared to the other samples, and suggesting that a secondary phase, such as surface contamination, may be present. A possible explanation for the reduced conductivity and increased activation energy could be surface contamination with Li_2CO_3, which can hinder lithium-ion transport and lead to poor overall conductivity. The conductivity study yielded results that are comparable to the literature. However, the observed differences in conductivity across the two sintering temperatures underscore the importance of optimising phase

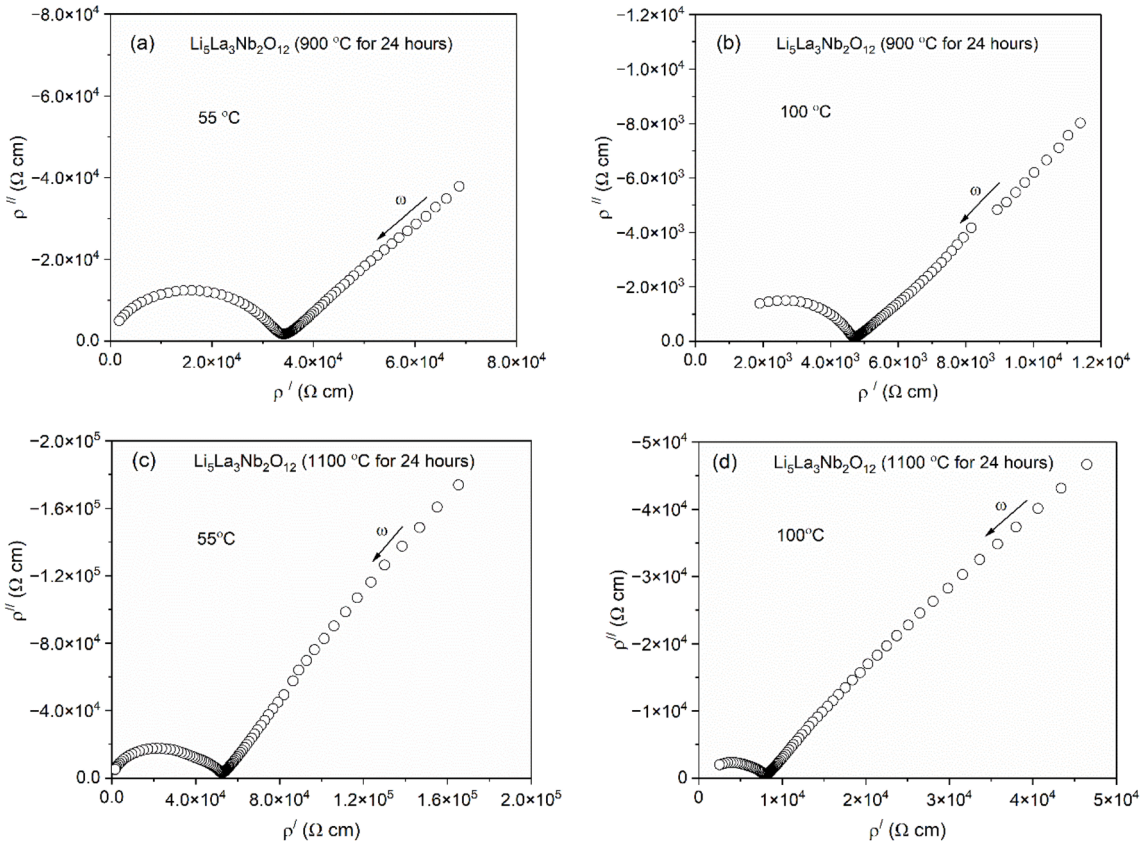

Fig. 11 Typical AC impedance plots obtained in the frequency range 5 Hz to 13 MHz using lithium ion blocking Au electrode for $Li_5La_3Nb_2O_{12}$ sintered at 900 °C (thickness: 0.15 cm; diameter: 1.3 cm), (a) 55 °C and (b) 100 °C and 1100 °C (thickness: 0.15 cm; diameter: 1.32 cm) (c) 55 °C and (d) 100 °C.

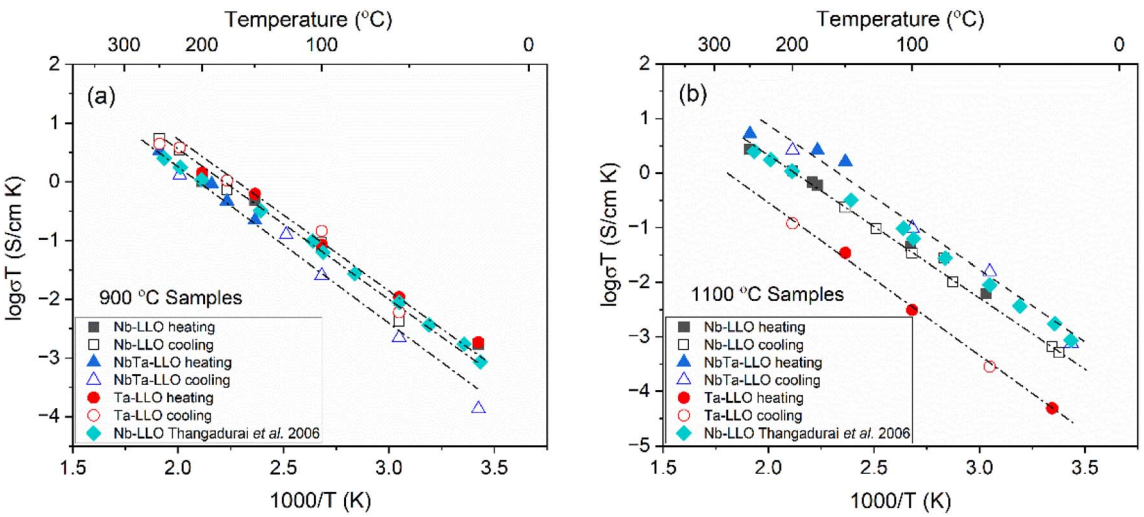

Fig. 12 Arrhenius plots of the total conductivity of all $Li_5La_3Nb_2O_{12}$ (Nb-LLO); $Li_5La_3Ta_2O_{12}$ (Ta-LLO); and $Li_5La_3NbTaO_{12}$ (NbTa-LLO) sintered at 900 °C (a) and sintered at 1100 °C (b). For comparison, data from literature[38] sintered at 1000 °C is included in both (a) and (b).

composition and structural features. To fully understand and control the conductivity behaviour in lithium garnet electrolytes, careful consideration of secondary phase (contamination) formation is required.

3.9 Lithium carbonate and alumina contamination

3.9.1 X-ray photoelectron spectroscopy. Initial evidence of lithium carbonate formation was observed through SEM and EDS imaging. Subsequent surface-sensitive XPS analysis

Table 2 Chemical composition, final synthesis temperature, Li ion conductivity and activation energy of Li_5-phase garnets from this study and the literature

Composition (final sintering temperature)	σ_{Li}^{+}(S cm^{-1})	E_a (eV)	References
$Li_5La_3Nb_2O_{12}$ (900 °C)	2.9×10^{-5} (55 °C; air)	0.43	This study
$Li_5La_3Nb_2O_{12}$ (1100 °C)	1.9×10^{-5} (55 °C; air)	0.44	This study
$Li_5La_3Nb_2O_{12}$ (950 °C)	2.3×10^{-5} (50 °C; air)	0.55	38
$Li_5La_3Nb_2O_{12}$ (950 °C)	8.0×10^{-6} (50 °C; air)	0.43	5
$Li_5La_3Nb_2O_{12}$ (950 °C)	2.5×10^{-7}(25 °C; air)	0.51	39
$Li_5La_3Nb_2O_{12}$ (1100 °C)	5.1×10^{-6} (22 °C; air)	0.60	40
$Li_5La_3NbTaO_{12}$ (900 °C)	6.8×10^{-6} (55 °C; air)	0.50	This study
$Li_5La_3NbTaO_{12}$ (1100 °C)	2.6×10^{-5} (55 °C; air)	0.45	This study
$Li_{3.43}La_3Nb_{1.07}Ta_{0.93}O_{12-y}$ (1000 °C)	7.1×10^{-8} (25 °C; air)	0.59	23
$Li_5La_3Ta_2O_{12}$ (900 °C)	3.3×10^{-5} (55 °C; air)	0.42	This study
$Li_5La_3Ta_2O_{12}$ (1100 °C)	8.6×10^{-7} (55 °C; air)	0.62	This study
$Li_5La_3Ta_2O_{12}$ (850 °C)	5.0×10^{-6} (40 °C; air)	0.55	41
$Li_5La_3Ta_2O_{12}$ (950 °C)	1.2×10^{-6} (50 °C; air)	0.56	5
$Li_5La_3Ta_2O_{12}$ (1000 °C)	2.6×10^{-6} (60 °C; air)	0.6	42
$Li_5La_3Bi_2O_{12}$ (775 °C)	4.0×10^{-5} (22 °C; Ar)	0.54	43
$Li_5La_3Sb_2O_{12}$ (950 °C)	8.2×10^{-6} (24 °C; Ar)	0.51	44

confirmed an excess of carbon and oxygen on the surfaces of all samples, consistent with the presence of Li_2CO_3. However, XPS analysis of the Li 1s region could not effectively distinguish between lithium in the carbonate and lithium in the garnet lattice due to overlapping binding energies.[45] Additionally, if the carbonate layer thickness is greater than the photoelectron escape depth (*ca.* 3.43 nm at a kinetic energy of 1432 eV),[46] then only the Li from the carbonate layer will be measured. However, this value must be considered indicative only, as the uniformity of the layer is very likely inhomogeneous, which is why the signals from the metals can be detected. Therefore, to investigate the carbonate presence further, a $Li_5La_3Nb_2O_{12}$ pellet was analysed under different conditions: (i) after being stored in a desiccator for approximately one month, and (ii) following heat treatment at 800 °C for two hours, then cooled to room temperature in a desiccator before measurement. Additionally, the sample was measured after heat treatment at 300 °C within the XPS measurement chamber. The results (Fig. 13) highlight that a change to the garnet pellet surface occurs as the C 1s and O 1s binding energy regions.

In the O 1s spectra, the carbonate oxygen peak at ~532 eV is significantly reduced after heat treatment, while the lattice oxygen peak associated with the garnet phase at ~529 eV becomes more prominent. Similarly, in the C 1s region, the carbonate carbon peak at ~290 eV and the atmospheric carbon peak at ~285 eV both diminish after heating.[47] Initially, XPS

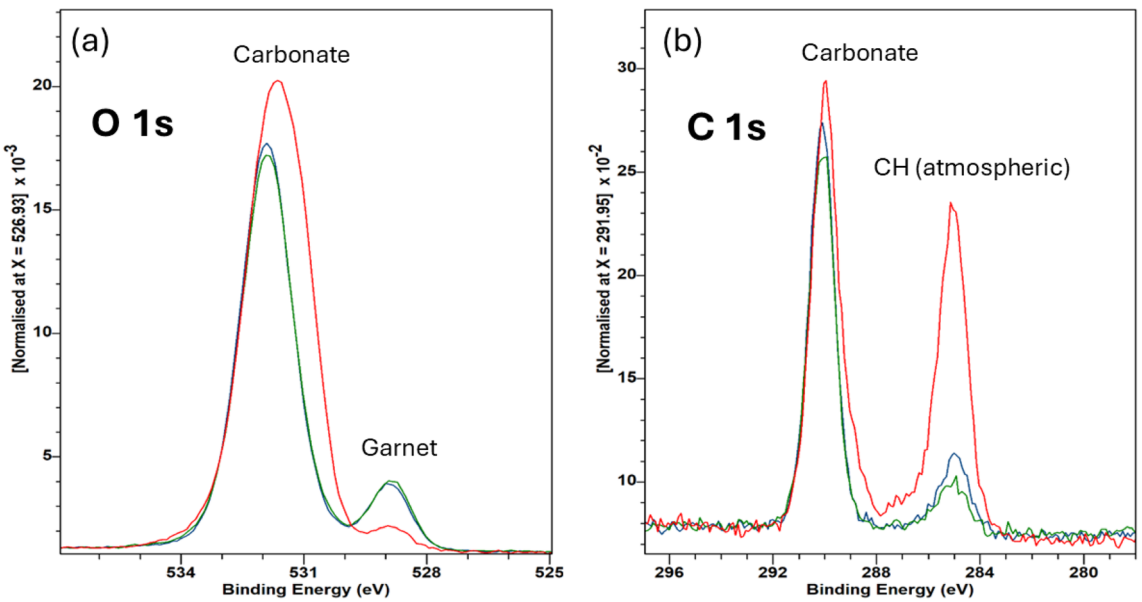

Fig. 13 XPS spectra for (a) O 1s and (b) C 1s regions of the surface of $Li_5La_3Nb_2O_{12}$ pellet, at room temperature without prior heat treatment (red line), at room temperature after heating the sample to 800 °C in air for 2 hours pre-measurement (green line) and at 300 °C for after heating the sample to 800 °C in air for 2 hours pre-measurement (blue line).

measurements were restricted to room temperature due to gas evolution that occurred on heating, which disrupted the vacuum at elevated temperatures. However, partial removal of the carbonate layer *via* heating enabled higher-temperature measurements by minimising decomposition-related outgassing.

In the sample without additional heat treatment, the XPS spectrum was dominated by Li_2CO_3, effectively masking signals from key garnet elements such as La and Nb. After heating, the carbonate layer was substantially reduced, revealing signals from the underlying garnet phase (Fig. S11, see SI). Based on the surface sensitivity of XPS and comparison with literature, the thickness of the surface Li_2CO_3 layer is estimated to be approximately 30 nm–100 nm.[15,48,49]

Although heating of the sample was effective in immediately reducing the carbonate layer, an order of tens of nanometres of carbonate remained, and the layer is expected to regrow over time due to continued surface reactions with atmospheric H_2O and CO_2. Since the carbonate layer was observed across all samples during XPS analysis on samples stored in the lab, it is likely that without removing this layer, the ionic conductivity was impacted due to the lithium-ion transport being impeded by the carbonate layer at the pellet surfaces. Fig. S12 (see SI) presents fractured cross-sectional SEM images of an Ar-treated pellet, stored in the dry room for 45 days, and an untreated pellet, stored for more than four months. The images reveal the extent of surface contamination, with a contamination layer of 50–120 nm in the former case and a thicker contamination layer of 500–800 nm in the latter (Fig. S12, see SI).

These findings emphasise the need for future focus on both the complete removal and prevention of surface carbonate formation. It was found that storing samples at room temperature in a desiccator in a dry room alone was insufficient. This area is growing interests, with strategies such as protective coatings, optimised atmospheres during synthesis, or post-synthesis carbonate layer control employed to mitigate excessive Li_2CO_3 formation and preserve the electrochemical performance of garnet-type solid electrolytes.[47,50–52]

3.9.2 Thermogravimetric analysis. TGA was employed to investigate the impact of heat treatment on the surface chemistry of the garnet pellets. In ambient atmosphere garnet samples undergo protonic exchange with water, as described in eqn (3).

$$Li_5La_3M_2O_{12} + H_2O \rightarrow \text{“}Li_{5-x}H_xLa_3M_2O_{12}\cdot xLiOH\text{”} \quad (3)$$

The protonic exchanged garnet subsequently reacts with carbon dioxide and forms a surface layer of lithium carbonate, as proposed in eqn (4).

$$Li_{5-x}H_xLa_3M_2O_{12}\cdot xLiOH + \frac{x}{2}CO_2 \rightarrow \text{“}Li_{5-x}La_3M_2O_{12-x/2}\cdot \frac{x}{2}Li_2CO_3\text{”} + H_2O \quad (4)$$

A TGA experiment was designed to replicate the thermal treatment applied to the XPS samples, by heating the previously synthesised (sintered at 1100 °C) $Li_5La_3M_2O_{12}$ (M = Nb, Ta, Nb/Ta) pellets to 800 °C for one hour, followed by cooling to 100 °C, with the cycle repeated once. All compositions (Fig. S13, see SI) exhibit three distinct weight loss events occurring at approximately 100 °C, 250 °C, and 550 °C, indicating a similar interaction with atmospheric species across all samples. These features are consistent with the behaviour reported in literature for garnet-type materials:[53,54]

- The first weight loss (~100 °C) corresponds to the desorption of surface-adsorbed water.
- The second (~250 °C) is attributed to the release of structural H_2O arising from proton incorporation into the garnet lattice.
- The third event (~550 °C) reflects the decomposition of surface Li_2CO_3, with the release of CO_2.

The ~250 °C water loss is attributed to H^+ ions substituting for Li^+ within the garnet structure, supporting the concept of a Li^+/H^+ exchange mechanism.[53] This mechanism, when coupled with exposure to ambient CO_2, results in the preformed LiOH layer reacting to form Li_2CO_3 on the surface (eqn (4)). Upon heating, the decomposition of the surface carbonate species is believed to occur *via* loss of carbon dioxide (eqn (5)), and the back-insertion of the lithium from lithium carbonate into the garnet returns to the original “stoichiometry”.

$$Li_{5-x}La_3M_2O_{12-x/2}\cdot \frac{x}{2}Li_2CO_3 \rightarrow \text{“}Li_5La_3M_2O_{12}\text{”} + \frac{x}{2}CO_2 \quad (5)$$

Importantly, the garnet reactions in ambient conditions are reversible, and at the end of the cycle, the original garnet is recovered.[55] Interestingly, during both heating cycles, a slight mass increase is observed between 100 and ~250 °C. This may reflect adsorption or formation of LiOH and Li_2CO_3 on the surface during heating from residual atmospheric amounts of water and carbon dioxide, which is subsequently lost at higher temperatures. This observation may suggest that carbonate formation is initiated during the cooling phase of synthesis,[56] particularly as the sample passes through the 100–250 °C range, where the reaction is thermodynamically favourable (Fig. 14). Additionally, the presence of unreacted lithium, intentionally added during synthesis to compensate for lithium volatilisation at high sintering temperatures, may contribute to the formation of surface Li_2CO_3. As the amount of excess lithium was not precisely optimised, residual reactive Li_2O within the structure may facilitate Li_2CO_3 formation upon exposure to ambient air. TGA analysis shows that heating the samples to 800 °C for one-hour results in a two-step decomposition of surface Li_2CO_3. This thermal behaviour aligns with the changes observed in the XPS spectra, confirming the progressive removal of carbonate species from the surface. Understanding the two-step Li_2CO_3 formation and decomposition process under ambient conditions is essential for guiding future efforts to optimise synthesis protocols, reduce surface contamination, and explore alternative strategies that mitigate carbonate formation more effectively than the current approach.

3.9.3 Reaction with the alumina crucible. *Ex situ* PXRD analysis was performed on the pellet which was in contact with alumina crucible to assess potential intrinsic Al-doping, which

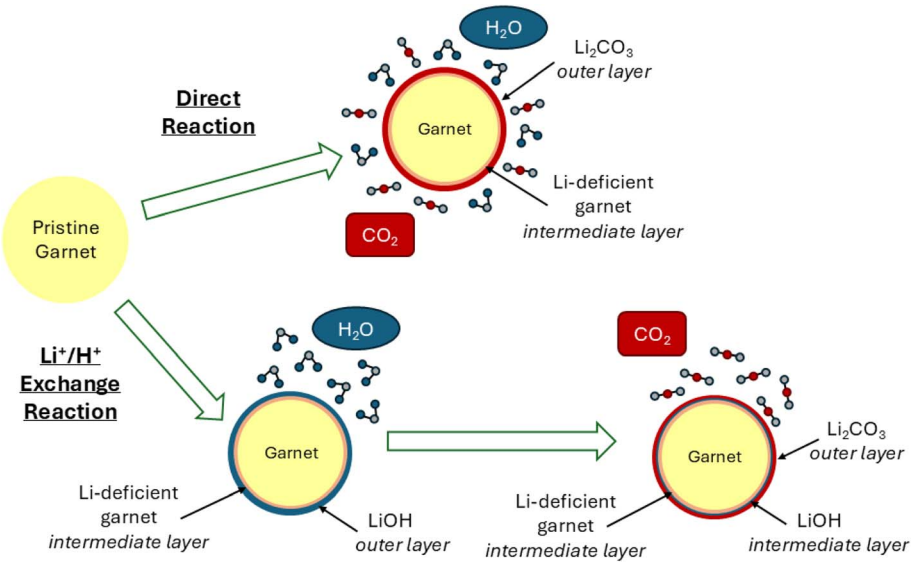

Fig. 14 Schematic representation of the two potential reaction pathways which describe the formation of Li_2CO_3 outer layer which forms on the garnet surface under ambient conditions. Top: direct reaction of both H_2O and CO_2 in one step, and bottom: two step exchange reaction, first with H_2O, followed by reaction with CO_2.

may have arisen from an interaction with crucibles during high-temperature sintering. Efforts were focused on conducting a more extensive study on the Nb-based garnet. The PXRD patterns of $Li_5La_3Nb_2O_{12}$ samples in Fig. 15 were synthesised under various conditions: with and without a sacrificial mother powder at 1100 °C for 24 hours, at 900 °C for 24 hours without a mother powder, and at 1100 °C for 40 hours without a mother powder. The ICSD reference pattern for $Li_5La_3Nb_2O_{12}$ (ICSD #18586) is included for comparison. Additionally, $LaAlO_3$ (ICSD #92554), marked with red asterisks, appears in the 1100 °C samples without mother powder, indicating the formation of this phase due to interfacial reaction with the alumina crucible.

From the *ex situ* PXRD patterns of $Li_5La_3Nb_2O_{12}$, it is evident that the sample sintered at 1100 °C with a sacrificial mother powder and the sample sintered at 900 °C without a mother powder both yield a clean, single-phase garnet structure. In contrast, the sample sintered at 1100 °C without a mother powder shows the garnet phase along with multiple impurity phases, one of which is identified as $LaAlO_3$. Notably, when the sintering time at 1100 °C is extended to 40 hours without a mother powder, the Al-based secondary phase becomes the dominant phase, indicating extensive reaction between the garnet and the alumina crucible. The PXRD analysis of $Li_5La_3Ta_2O_{12}$ and $Li_5La_3NbTaO_{12}$ (Fig. S14 and S15, see SI) sintered without mother powder at 900 °C and 1100 °C, also shows the presence of a major secondary phase in the base pellet sintered at 1100 °C in the alumina crucible.

Al has been widely employed to stabilise cubic phase garnets, both doping intrinsically *via* alumina crucibles,[57–59] or doping extrinsically *via* the addition of alumina,[60–62] where Al substitutes into the structure in place of Li. This substitution creates charge-compensating lithium vacancies, which are essential for stabilising the high-conductivity cubic phase.[58] Al_2O_3 has been employed directly as both a sintering aid and phase stabiliser in the synthesis of garnet-type materials such as $Li_7La_3Zr_2O_{12}$ (LLZO).[62,63] Al_2O_3 promotes densification by forming a secondary phase at grain boundaries, which has been shown to suppress lithium dendrite growth and enhance overall ionic conductivity.[64] The process of intrinsic doping happens at high sintering temperatures, when reactive species, such as Li_2O or La_2O_3 can interact with the crucible, producing transient melt phases capable of dissolving Al_2O_3.[58] This process facilitates the diffusion of Al into the garnet, leading to the formation of secondary Al-containing phases.[65] In addition, it has been

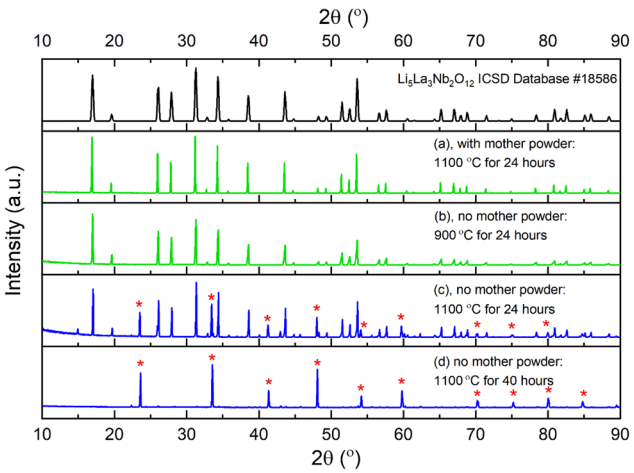

Fig. 15 *Ex situ* PXRD patterns of $Li_5La_3Nb_2O_{12}$ pellet in contact with alumina crucible during sintering at (a) 1100 °C for 24 hours with sacrificial mother powder, (b) 900 °C for 24 hours without mother powder, (c) 1100 °C for 24 hours without mother powder, and (d) 1100 °C for 40 hours without mother powder. For comparison, ICSD $Li_5La_3Nb_2O_{12}$ (#18586) is given, and *denotes the $LaAlO_3$ (#92554) phase.

shown that one significant reason for reaction of garnet with the crucible during high temperature sintering is the Li volatilization inducing Al-doping to ensure charge balance.[66]

A previous study on LLZO garnets reported that reactions between the garnet and alumina crucibles begin around at ~1050 °C.[67] This aligns with our observations, where Al-containing phase $LaAlO_3$ emerges as a major phase in samples sintered without mother powder at 1100 °C but is only minor in the sample sintered at 900 °C. These results highlight the sensitivity of garnet materials to sintering conditions, particularly the role of temperature in driving Al contamination from the crucible. Careful control over sintering environments is therefore essential to ensure phase purity and material stoichiometry. To minimise Al contamination, two effective strategies are demonstrated in this study: (i) lowering the sintering temperature below 1100 °C, which reduces alumina crucible interaction, though it may compromise pellet densification, and (ii) utilising a sacrificial mother powder, which acts as a protective buffer layer, enabling clean garnet formation even at elevated temperatures. Overall, Al-related secondary phases were only observed in the base pellet in direct contact with the crucible, therefore strongly indicating that Al diffusion and contamination are surface-limited and driven by physical contact during sintering. Using single-crystal sapphire tubes for synthesis during *in situ* PXRD measurements allowed to avoid the Al contamination of the material due to the considerably lower reactivity of the alumina single crystal surface.

The BSE images of all the analogues sintered at 900 °C and 1100 °C without mother powder for 24 h are presented in Fig. 16. As also observed before from the PXRD analysis, the pellets in contact with the crucible during sintering at 900 °C show no evidence of secondary phases for all garnets. However, sintering at 1100 °C led to the formation of Al-rich phases, most severely in the case of Nb-doped garnets. Line and point EDS analysis of $Li_5La_3Nb_2O_{12}$ sintered at 1100 °C (Fig. S16 and S17, see SI) reveals the most significant reaction with the alumina crucible. Three distinct phases are observed: the garnet with the targeted stoichiometry, an Al- and La-rich phase, and a Nb-rich phase. This highlights the severe destabilisation of the garnet due to Al contamination from the crucible, forming a $LaAlO_3$ phase, as confirmed by XRD analysis.

Fig. S18 and S19 (see SI), show similar analyses for $Li_5La_3NbTaO_{12}$ and $Li_5La_3Ta_2O_{12}$. For $Li_5La_3NbTaO_{12}$, three phases are present: the intended garnet, a Ta- and Nb-rich phase, and an Al-rich phase containing minor La. This indicates notable, though less severe, interaction with the crucible compared to the Nb-based sample. $Li_5La_3Ta_2O_{12}$ exhibits the least contamination, with only two phases detected: the garnet and an Al- and La-rich secondary phase. These findings demonstrate that Nb-based garnets are more prone to crucible interactions at temperatures above 900 °C, owing to the greater tendency of niobium to undergo reduction at high temperatures.

Combining the findings from PXRD, SEM, and EDS, it is evident that sintering at 1100 °C without sacrificial mother powder leads to the formation of secondary La–Al phases. This effect is intensified with prolonged sintering durations, as the 40-hours sample predominantly shows La–Al phase formation. As established earlier, achieving a single-phase garnet at 1100 °C requires the use of sacrificial mother powder. Beyond phase control, SEM analysis confirms that this approach also promotes better densification and reduces surface voids compared to samples prepared without a mother powder.

Future approaches to achieve highly dense solid electrolytes at elevated temperatures are the use of ZrO_2, MgO or Pt crucibles, as they provide higher control on elemental composition of produced garnet,[68] especially the latter two show lower reactivity with the Li_2O gas.[69] For example, it was shown by Jiang *et al.*[70] that a smaller amount of Mg was incorporated in the Ga-doped LLZO structure at the same conditions of heat

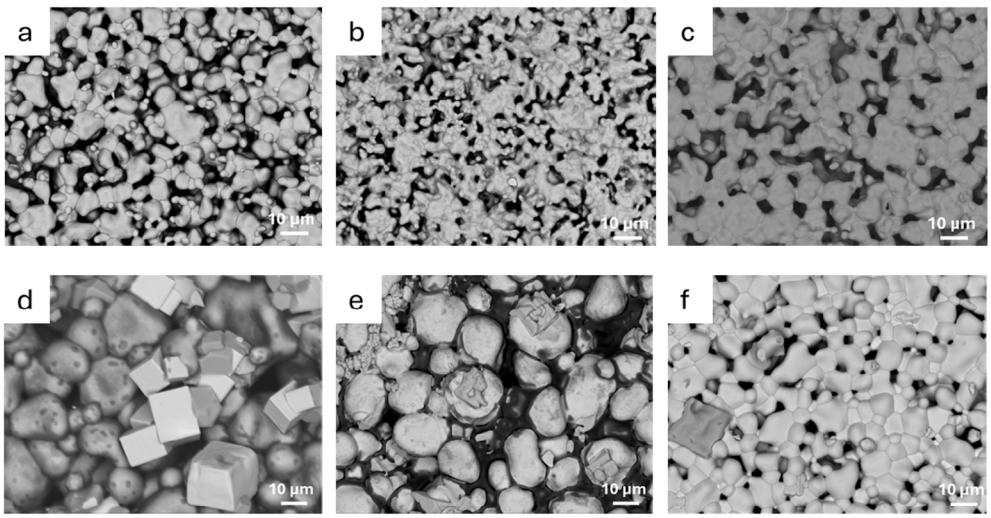

Fig. 16 Backscattered electron detector (BSED) SEM images of the base pellets in contact with alumina crucible sintered at 900 °C (a) $Li_5La_3Nb_2O_{12}$, (b) $Li_5La_3NbTaO_{12}$, and (c) $Li_5La_3Ta_2O_{12}$ and 1100 °C (d) $Li_5La_3Nb_2O_{12}$, (e) $Li_5La_3NbTaO_{12}$, and (f) $Li_5La_3Ta_2O_{12}$. Increased density was observed at 1100 °C.

treatment compared to Al. Alternatively, lower sintering temperatures or lower needed dwelling time at higher temperatures may be employed through advanced techniques such as ultra-fast high-temperature sintering,[71] flash sintering,[72] cold sintering[73] or spark plasma sintering[74,75] which can enable densification while minimizing contamination.[68,76]

3.9.4 Solid-state NMR spectroscopy. The ^{27}Al MAS NMR spectra of $Li_5La_3M_2O_{12}$ (M = Nb, Ta, Nb/Ta) in Fig. 17 offer an insight into the Al environments within the base pellets sintered at 1100 °C. Aluminium incorporation is observed across the samples, with all three compositions exhibiting a prominent resonance at ~11 ppm and a weaker resonance at ~77 ppm.

The high intensity resonance at ~11 ppm, characteristic of octahedrally coordinated Al, can be assigned to $LaAlO_3$,[40] which is consistent with previous PXRD, SEM, and EDS results. Alongside this dominant peak, all samples exhibit a lower intensity resonance at ~77 ppm, falling within the expected range for tetrahedrally coordinated aluminates (50–90 ppm).[77] A study by Vema *et al.*[62] identified a similar resonance at ~79 ppm when investigating Al-doped LLZO, attributing it to γ-$LiAlO_2$, therefore, the ~77 ppm peak observed here could likely correspond to the same phase. Additionally, the Ta-only sample shows a low-intensity resonance at ~67 ppm. Vema *et al.* also reported that a resonance at ~68 ppm arises from Al substitution into the Li 24 d site in the garnet structure, this suggests that the resonance slightly above the noise in the Ta sample may reflect minor Al doping into the garnet lattice.[62] Similar observations were reported by Karasulu *et al.*,[10] whose DFT calculations demonstrated that Al preferentially occupies the Li1 site, giving rise to an NMR shift of ~68.6 ppm and the observed NMR peak broadening originates from local structural distortions of the AlO_4 tetrahedra, where the absence of corner-sharing LiO_4 (Li2) neighbours increases the distortion index and thereby increasing the quadrupolar coupling constant.

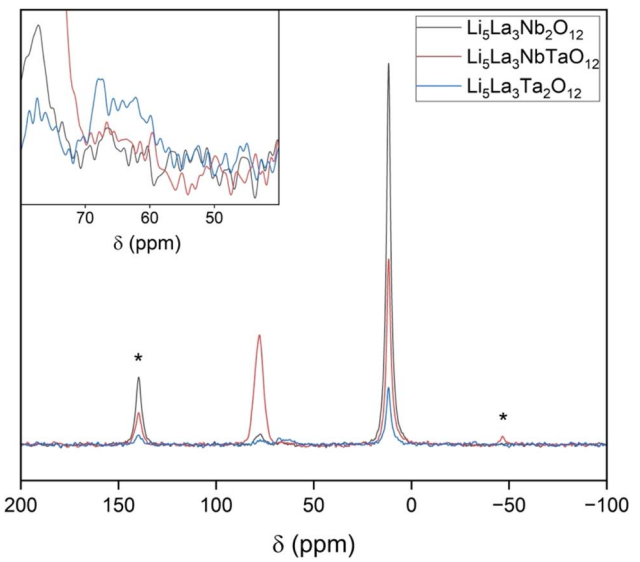

Fig. 17 Quantitative ^{27}Al (14.1 T, 20 kHz MAS) MAS NMR spectra of powder $Li_5La_3M_2O_{12}$ (M = Nb, Ta, Nb/Ta). The NMR spectra are shown normalised by the sample mass. The * symbol indicates spinning sidebands.

The ^{27}Al MAS NMR spectra were normalised by the sample mass in the rotor, allowing qualitative conclusions about the composition with the most Al-secondary phase to be drawn. The peak at ~11 ppm, associated with $LaAlO_3$, shows the greatest intensity in the Nb-only sample, followed by the mixed Nb/Ta, and the lowest in the Ta-only sample. This trend suggests that the Nb-only sample contains the highest concentration of $LaAlO_3$ secondary phase, which aligns with the SEM and EDS analysis of the base pellets. Interestingly, the trend does not hold for the low-intensity peaks. The mixed Nb/Ta sample exhibits the most intense resonance at ~77 ppm, suggesting it contains the most γ-$LiAlO_2$. The solid-state NMR spectroscopy study indicates that aluminium incorporation from the alumina crucible is present across all compositions, predominantly in an octahedral $LaAlO_3$ environment, with the Nb-only sample containing the most secondary phase in the samples studied. This implies that Nb promotes greater reactivity with alumina crucibles. However, as the Li stoichiometry was not precisely determined and conclusions regarding Al incorporation mechanisms remain incomplete. As a study by Lan *et al.* indicates that Li content strongly influences Al uptake,[67] therefore, further analysis of the sample stoichiometry is required to determine whether M-site substitution is driving Al contamination.

4. Conclusions

The parent garnet-type $Li_5La_3M_2O_{12}$ (M = Nb, Ta, Nb/Ta) was successfully synthesised *via* solid-state reaction at 900 °C and 1100 °C. Powder XRD and Raman spectroscopy confirmed single-phase garnets with $Ia\bar{3}d$ symmetry. SEM imaging showed better densification of the samples sintered at 1100 °C, than those sintered at 900 °C. The *in situ* PXRD study of the $Li_5La_3Nb_2O_{12}$ garnet gave an insight into the route of the phase formation. Under the conditions studied, the Nb garnet phase proceeds *via* La_2LiNbO_6, Li_3NbO_4 and La_3NbO_7, and the product begins to form below 700 °C. The investigation clearly highlighted that at elevated temperatures, above 1075 °C, decomposition of the garnet phase begins, and on the *in situ* scale, the product was almost entirely decomposed. This study identifies that such elevated temperatures to achieve the garnet structure is not the most efficient and that a lower temperature for a longer dwelling time may be sufficient.

It was observed that samples sintered at 900 °C showed similar conductivities to each other, while those sintered at 1100 °C displayed more variation between the garnet compositions. The highest conductivity measured in this study was 4.8 × 10^{-5} S cm^{-1} at 55 °C, for $Li_5La_3NbTaO_{12}$ sintered at 1100 °C. This is comparable to Li_5 phases previously reported in the literature.[35] ^{7}Li MAS NMR spectra showed a single resonance for all samples, indicating that all Li environments are equivalent due to fast Li-ion hopping, rendering the Li environments indistinguishable. ^{27}Al MAS NMR spectra revealed Al incorporation from alumina crucibles, in all samples sintered directly on the crucible base at 1100 °C. The main contaminant phase

appears to be $LaAlO_3$, which was confirmed by PXRD, SEM, and EDS analysis. This work showed that to reduce Al contamination, sintering with a sacrificial mother powder or at 900 °C is recommended. This study provides a comprehensive analysis of the Li_5- garnet phase, a composition often overlooked in favour of the more commonly studied $Li_7La_3Zr_2O_{12}$ (LLZO). By revisiting the parent garnet structure, this work offers valuable insights that could inform the design and optimisation of next-generation garnet-based solid-state lithium-ion electrolytes.

Author contributions

Heather A. Ritchie: conceptualisation, synthesis, formal analysis, investigation, methodology, validation, visualisation, writing – original draft; Ioanna M. Pateli: Raman and SEM data curation, formal analysis, investigation, methodology, writing, review & editing; Oxana V. Magdysyuk: PXRD data curation, formal analysis, investigation, methodology, writing, review & editing. Aaron B. Naden: TEM data curation, formal analysis, investigation, methodology, review & editing. Heitor S. Seleghini: data curation, review & editing; Federico Grillo: XPS data curation, formal analysis, investigation, methodology, review & editing. Gavin Peters: data curation; Sharon E. Ashbrook: collaboration, review & editing. John T. S. Irvine: collaboration and review; Venkataraman Thangadurai: conceptualisation, supervision, methodology, writing, review & editing.

Conflicts of interest

There are no conflicts to declare.

Data availability

The research data underpinning this publication, including X-ray diffraction, scanning electron microscopy, transmission electron microscopy, Raman spectroscopy, XPS spectroscopy, NMR spectroscopy, TGA analysis and EIS data are available at the University of St Andrews repository and can be accessed at **https://doi.org/10.17630/ddf38307-f6c1-4e66-ac13-f42fbd8c775e**.

Supplementary information: X-ray diffraction, scanning electron microscopy and elemental analysis, XPS spectroscopy, TGA analysis and electrochemical impedance data. See DOI: **https://doi.org/10.1039/d5ta06905j**.

Acknowledgements

We also acknowledge the support from EPSRC Core Equipment Grant (EP/V034138/1) for powder diffractometers and the support from the EPSRC Light Element Analysis Facility Grant EP/T 0192981 and the EPSRC Strategic Equipment Resource Grant EP/R 023751/1 for the Raman spectrometer and Scanning electron microscope. We gratefully acknowledge support from the EPSRC through grant numbers EP/L017008/1, EP/R023751/1 and EP/T019298/1 for scanning transmission electron microscope data. H. S. S. thanks the Allan Handsel Postgraduate Research Scholarship. V. T. also thanks University of St Andrews for Chair in Energy.

References

1 J. B. Goodenough, *Energy Environ. Sci.*, 2014, **7**, 14–18.
2 V. Thangadurai, *ACS Energy Lett.*, 2025, **10**, 5067–5074.
3 J. Janek and W. G. Zeier, *Nat. Energy*, 2016, **1**, 1–4.
4 V. Thangadurai, S. Narayanan and D. Pinzaru, *Chem. Soc. Rev.*, 2014, **43**, 4714–4727.
5 V. Thangadurai, H. Kaack and W. J. F. Weppner, *J. Am. Ceram. Soc.*, 2003, **86**, 437–440.
6 E. J. Cussen, *Chem. Commun.*, 2006, 412–413.
7 B. Dong, M. P. Stockham, P. A. Chater and P. R. Slater, *Dalton Trans.*, 2020, **49**, 11727–11735.
8 V. Thangadurai and W. Weppner, *Adv. Funct. Mater.*, 2005, **15**, 107–112.
9 R. Murugan, V. Thangadurai and W. Weppner, *Angew. Chem., Int. Ed.*, 2007, **46**, 7778–7781.
10 B. Karasulu, S. P. Emge, M. F. Groh, C. P. Grey and A. J. Morris, *J. Am. Chem. Soc.*, 2020, **142**, 3132–3148.
11 J. Awaka, N. Kijima, H. Hayakawa and J. Akimoto, *J. Solid State Chem.*, 2009, **182**, 2046–2052.
12 Y. Mao, J. Liu, W. Chen, W. Zhang and C. Sun, *Mater. Horitz.*, 2025, **12**, 6082–6123.
13 A. J. Samson, K. Hofstetter, S. Bag and V. Thangadurai, *Energy Environ. Sci.*, 2019, **12**, 2957–2975.
14 K. Ma, B. Chen, C. X. Li and V. Thangadurai, *J. Mater. Chem. A*, 2023, **12**, 3601–3615.
15 H. Huo, J. Luo, V. Thangadurai, X. Guo, C. W. Nan and X. Sun, *ACS Energy Lett.*, 2020, **5**, 252–262.
16 L. Xu, J. Li, W. Deng, H. Shuai, S. Li, Z. Xu, J. Li, H. Hou, H. Peng, G. Zou and X. Ji, *Adv. Energy Mater.*, 2021, **11**, 1–24.
17 A. A. Coelho, *J. Appl. Crystallogr.*, 2018, **51**, 210–218.
18 H. Rietveld, *J. Appl. Crystallogr.*, 1969, **2**, 65–71.
19 H. Rietveld, *Acta Crystallogr.*, 1967, **22**, 151–152.
20 N. Fairley, V. Fernandez, M. Richard-Plouet, C. Guillot-Deudon, J. Walton, E. Smith, D. Flahaut, M. Greiner, M. Biesinger, S. Tougaard, D. Morgan and J. Baltrusaitis, *Appl. Surf. Sci. Adv.*, 2021, **5**, 100112.
21 Y. Seto and M. Ohtsuka, *J. Appl. Crystallogr.*, 2022, **55**, 397–410.
22 R. D. Shannon, *Acta Crystallogr.*, 1976, **32**, 751–761.
23 A. P. Kafle, W. Wong-Ng, V. Oleshko, G. R. Stafford, J. A. Kaduk, A. Eufrasio, I. L. Pegg and B. Dutta, *Powder Diffr.*, 2024, **39**, 191–205.
24 K. Hu, H. Tang, B. Zheng, L. Yu, F. Xiong, H. Li, L. Qiu, F. Wan, Y. Song, B. Zhong, Z. Wu and X. Guo, *Angew. Chem., Int. Ed.*, 2025, **64**, e202413563.
25 F. Tietz, T. Wegener, M. T. Gerhards, M. Giarola and G. Mariotto, *Solid State Ionics*, 2013, **230**, 77–82.
26 J. T. S. Irvine, D. C. Sinclair and A. R. West, *Adv. Mater.*, 1990, **2**, 132–138.
27 Y. Huang, H. Yang, Y. Gao, G. Chen, Y. Li, L. Shi and D. Zhang, *Mater. Chem. Front.*, 2024, **8**, 1282–1299.
28 A. Sharafi, E. Kazyak, A. L. Davis, S. Yu, T. Thompson, D. J. Siegel, N. P. Dasgupta and J. Sakamoto, *Chem. Mater.*, 2017, **29**, 7961–7968.
29 H. Buschmann, J. Dölle, S. Berendts, A. Kuhn, P. Bottke, M. Wilkening, P. Heitjans, A. Senyshyn, H. Ehrenberg,

A. Lotnyk, V. Duppel, L. Kienle and J. Janek, *Phys. Chem. Chem. Phys.*, 2011, **13**, 19378–19392.
30 C. D. Wagner, W. M. Kiggs, L. E. Davis and J. F. Moulder, *Handbook of X-Ray Photoelectron Spectroscopy*, Perkin-Elmer Corporation-Physical Electronics Division, Eden Prairie, MN, 1979.
31 NIST X-ray Photoelectron Spectroscopy Database (SRD 20), **https://srdata.nist.gov/xps/%0A**.
32 M. F. Sunding, K. Hadidi, S. Diplas, O. M. Løvvik, T. E. Norby and A. E. Gunnæs, *J. Electron Spectrosc. Relat. Phenom.*, 2011, **184**, 399–409.
33 A. Müller, F. Okur, A. Aribia, N. Osenciat, C. A. F. Vaz, V. Siller, M. El Kazzi, E. Gilshtein, M. H. Futscher, K. V. Kravchyk, M. V. Kovalenko and Y. E. Romanyuk, *Mater. Adv.*, 2023, **4**, 2138–2146.
34 H. Yamada, T. Ito, S. P. Kammampata and V. Thangadurai, *ACS Appl. Mater. Interfaces*, 2020, **12**, 36119–36127.
35 T. Pang, S. Wu, H. Wu, X. Li, Y. Li, L. T. Yu, H. Zhang, Y. Han, Z. Guo and N. Zhang, *Adv. Sci.*, 2025, **12**, e04388.
36 E. J. Cussen, *J. Mater. Chem.*, 2010, **20**, 5167–5173.
37 L. Van Wüllen, T. Echelmeyer, H. W. Meyer and D. Wilmer, *Phys. Chem. Chem. Phys.*, 2007, **9**, 3298–3303.
38 V. Thangadurai and W. Weppner, *J. Solid State Chem.*, 2006, **179**, 974–984.
39 L. Truong and V. Thangadurai, *Chem. Mater.*, 2011, **23**, 3970–3977.
40 S. Narayanan and V. Thangadurai, *J. Power Sources*, 2011, **196**, 8085–8090.
41 C. R. Mariappan, K. I. Gnanasekar, V. Jayaraman and T. Gnanasekaran, *J. Electroceram.*, 2013, **30**, 258–265.
42 H. El-Shinawi and S. M. El-Dafrawy, *J. Solid State Chem.*, 2025, **343**, 125154.
43 R. Murugan, W. Weppner, P. Schmid-Beurmann and V. Thangadurai, *Mater. Sci. Eng., B*, 2007, **143**, 14–20.
44 R. Murugan, W. Weppner, P. Schmid-Beurmann and V. Thangadurai, *Mater. Res. Bull.*, 2008, **43**, 2579–2591.
45 M. Fingerle, C. Loho, T. Ferber, H. Hahn and R. Hausbrand, *J. Power Sources*, 2017, **366**, 72–79.
46 S. Tanuma, C. J. Powell and D. R. Penn, *Surf. Interface Anal.*, 1994, **21**, 165–176.
47 P. Srivastava, B. Bazri, D. K. Maurya, Y. T. Hung, D. H. Wei and R. S. Liu, *ACS Energy Lett.*, 2025, **10**, 1725–1732.
48 L. Cheng, C. H. Wu, A. Jarry, W. Chen, Y. Ye, J. Zhu, R. Kostecki, K. Persson, J. Guo, M. Salmeron, G. Chen and M. Doeff, *ACS Appl. Mater. Interfaces*, 2015, **7**, 17649–17655.
49 L. Cheng, E. J. Crumlin, W. Chen, R. Qiao, H. Hou, S. Franz Lux, V. Zorba, R. Russo, R. Kostecki, Z. Liu, K. Persson, W. Yang, J. Cabana, T. Richardson, G. Chen and M. Doeff, *Phys. Chem. Chem. Phys.*, 2014, **16**, 18294–18300.
50 N. Wang, M. Jia, Z. Bi and X. Guo, *Adv. Funct. Mater.*, 2024, **34**, 2401400.
51 X. Yi, Y. Guo, S. Chi, S. Pan, C. Geng, M. Li, Z. Li, W. Lv, S. Wu and Q. H. Yang, *Adv. Funct. Mater.*, 2023, **33**, 2303574.
52 Y. N. Yang, Y. X. Li, Y. Q. Li and T. Zhang, *Nat. Commun.*, 2020, **11**, 5519.
53 A. Sharafi, S. Yu, M. Naguib, M. Lee, C. Ma, H. M. Meyer, J. Nanda, M. Chi, D. J. Siegel and J. Sakamoto, *J. Mater. Chem. A*, 2017, **5**, 13475–13487.
54 H. Huo, J. Luo, V. Thangadurai, X. Guo, C. W. Nan and X. Sun, *ACS Energy Lett.*, 2020, **5**, 252–262.
55 G. Larraz, A. Orera and M. L. Sanjuán, *J. Mater. Chem. A*, 2013, **1**, 11419–11428.
56 R. Wagner, D. Rettenwander, G. J. Redhammer, G. Tippelt, G. Sabathi, M. E. Musso, B. Stanje, M. Wilkening, E. Suard and G. Amthauer, *Inorg. Chem.*, 2016, **55**, 12211–12219.
57 Y. Shimonishi, A. Toda, T. Zhang, A. Hirano, N. Imanishi, O. Yamamoto and Y. Takeda, *Solid State Ionics*, 2011, **183**, 48–53.
58 C. A. Geiger, E. Alekseev, B. Lazic, M. Fisch, T. Armbruster, R. Langner, M. Fechtelkord, N. Kim, T. Pettke and W. Weppner, *Inorg. Chem.*, 2011, **50**, 1089–1097.
59 M. A. Limpert, T. B. Atwater, T. Hamann, G. L. Godbey, G. T. Hitz, D. W. McOwen and E. D. Wachsman, *Chem. Mater.*, 2022, **34**, 9468–9478.
60 S. Kumazaki, Y. Iriyama, K. H. Kim, R. Murugan, K. Tanabe, K. Yamamoto, T. Hirayama and Z. Ogumi, *Electrochem. Commun.*, 2011, **13**, 509–512.
61 J. Sastre, T. Y. Lin, A. N. Filippin, A. Priebe, E. Avancini, J. Michler, A. N. Tiwari, Y. E. Romanyuk and S. Buecheler, *ACS Appl. Energy Mater.*, 2019, **2**, 8511–8524.
62 S. Vema, A. H. Berge, S. Nagendran and C. P. Grey, *Chem. Mater.*, 2023, **35**, 9632–9646.
63 Y. Suzuki, K. Kami, K. Watanabe, A. Watanabe, N. Saito, T. Ohnishi, K. Takada, R. Sudo and N. Imanishi, *Solid State Ionics*, 2015, **278**, 172–176.
64 X. Hu, S. Chen, Z. Wang, Y. Chen, B. Yuan, Y. Zhang, W. Liu and Y. Yu, *Nano Lett.*, 2023, **23**, 887–894.
65 E. Rangasamy, J. Wolfenstine and J. Sakamoto, *Solid State Ionics*, 2012, **206**, 28–32.
66 B. Dong, L. L. Driscoll, M. P. Stockham, E. Kendrick and P. R. Slater, *Solid State Ionics*, 2020, **350**, 115317.
67 W. Lan, D. Lu, R. Zhao and H. Chen, *Int. J. Electrochem. Sci.*, 2019, **14**, 9695–9703.
68 C. Chen, K. Wang, H. He, E. Hanc, M. Kotobuki and L. Lu, *Small*, 2023, **19**, 1–33.
69 X. Huang, Y. Lu, H. Guo, Z. Song, T. Xiu, M. E. Badding and Z. Wen, *ACS Appl. Energy Mater.*, 2018, **1**, 5355–5365.
70 Y. Jiang, Y. Zhou, Z. Hu, Y. Huang and X. Zhu, *Ceram. Int.*, 2020, **46**, 3367–3373.
71 A. Kern and P. J. McGinn, *J. Eur. Ceram. Soc.*, 2022, **42**, 7501–7507.
72 Y. Yang, Z. Zhang, T. Ma, S. Jia and C. Huang, *Ionics*, 2025, **31**, 1341–1350.
73 J. H. Seo, H. Nakaya, Y. Takeuchi, Z. Fan, H. Hikosaka, R. Rajagopalan, E. D. Gomez, M. Iwasaki and C. A. Randall, *J. Eur. Ceram. Soc.*, 2020, **40**, 6241–6248.
74 M. Kotobuki and M. Koishi, *J. Alloys Compd.*, 2020, **826**, 154213.
75 S. Palakkathodi Kammampata, H. Yamada, T. Ito, R. Paul and V. Thangadurai, *J. Mater. Chem. A*, 2020, **8**, 2581–2590.
76 A. Sazvar, M. Hajibandeh, P. Vafaei, E. Hosseinzadeh and M. Jabbari, *J. Energy Storage*, 2024, **101**, 113863.
77 M. Haouas, F. Taulelle and C. Martineau, *Prog. Nucl. Magn. Reson. Spectrosc.*, 2016, **94–95**, 11–36.